

This is an Open Access document downloaded from ORCA, Cardiff University's institutional repository: <https://orca.cardiff.ac.uk/id/eprint/176546/>

This is the author's version of a work that was submitted to / accepted for publication.

Citation for final published version:

Lissenberg, C. Johan , McCaig, Andrew M., Lang, Susan Q., Blum, Peter, Abe, Natsue, Brazelton, William J., Coltat, Rémi, Deans, Jeremy R., Dickerson, Kristin L., Godard, Marguerite, John, Barbara E., Klein, Frieder, Kuehn, Rebecca, Lin, Kuan-Yu, Liu, Haiyang, Lopes, Ethan L., Nozaka, Toshio, Parsons, Andrew J., Pathak, Vamdev, Reagan, Mark K., Robare, Jordyn A., Savov, Ivan P., Schwarzenbach, Esther M., Sissmann, Olivier J., Southam, Gordon, Wang, Fengping, Wheat, C. Geoffrey, Anderson, Lesley and Treadwell, Sarah 2024. A long section of serpentinized depleted mantle peridotite. *Science* 385 (6709) , pp. 623-629. 10.1126/science.adp1058

Publishers page: <http://dx.doi.org/10.1126/science.adp1058>

Please note:

Changes made as a result of publishing processes such as copy-editing, formatting and page numbers may not be reflected in this version. For the definitive version of this publication, please refer to the published source. You are advised to consult the publisher's version if you wish to cite this paper.

This version is being made available in accordance with publisher policies. See <http://orca.cf.ac.uk/policies.html> for usage policies. Copyright and moral rights for publications made available in ORCA are retained by the copyright holders.



A long section of serpentized depleted mantle peridotite

C. Johan Lissenberg^{1*}, Andrew M. McCaig², Susan Q. Lang³, Peter Blum⁴, Natsue Abe⁵, William J. Brazelton⁶, Rémi Coltat⁷, Jeremy R. Deans⁸, Kristin L. Dickerson⁹, Marguerite Godard¹⁰, Barbara E. John¹¹, Frieder Klein¹², Rebecca Kuehn¹³, Kuan-Yu Lin¹⁴, Haiyang Liu¹⁵, Ethan L. Lopes¹⁶, Toshio Nozaka¹⁷, Andrew J. Parsons¹⁸, Vamdev Pathak¹⁹, Mark K. Reagan²⁰, Jordyn A. Robare²¹, Ivan P. Savov², Esther M. Schwarzenbach²², Olivier J. Sissmann²³, Gordon Southam²⁴, Fengping Wang²⁵, C. Geoffrey Wheat²⁶, Lesley Anderson²⁷, Sarah Treadwell²⁸

¹School of Earth and Environmental Sciences, Cardiff University; Cardiff, United Kingdom.

²School of Earth and Environment, University of Leeds; Leeds, United Kingdom

³Department of Geology and Geophysics, Woods Hole Oceanographic Institution; Woods Hole MA USA.

⁴International Ocean Discovery Program, Texas A&M University; College Station TX, USA.

⁵Japan Agency for Marine-Earth Science and Technology; Yokohama, Japan.

⁶School of Biological Sciences, University of Utah; Salt Lake City UT, USA.

⁷Geosciences Department, Ecole Normale Supérieure; Paris, France and Instituto Andaluz de Ciencias de la Tierra; CSIC-UGR, Spain.

⁸School of Biological, Environmental, and Earth Sciences, University of Southern Mississippi; Hattiesburg MS, USA.

⁹Department of Earth and Planetary Sciences, University of California, Santa Cruz; Santa Cruz CA, USA.

¹⁰Geosciences Montpellier, CNRS, University of Montpellier, Montpellier, France.

¹¹Department of Geology and Geophysics, University of Wyoming; Laramie WY, USA.

¹²Department of Marine Chemistry and Geochemistry, Woods Hole Oceanographic Institution; Woods Hole MA, USA.

¹³Institute of Geosciences and Geography, Martin-Luther-University Halle-Wittenberg; Halle, Germany.

¹⁴Department of Earth Sciences, University of Delaware; Newark DE, USA.

¹⁵Center of Deep Sea Research, Institute of Oceanology, Chinese Academy of Sciences; Qingdao, China.

¹⁶Department of Geophysics, Stanford University; Stanford CA, USA.

¹⁷Department of Earth Sciences, Okayama University; Okayama, Japan.

¹⁸School of Geography, Earth and Environmental Sciences, University of Plymouth; Plymouth, United Kingdom.

¹⁹Department of Geology, Central University of Punjab; Bathinda, India.

²⁰Department of Earth and Environmental Sciences, University of Iowa; Iowa City IA, USA.

²¹School of Molecular Sciences, Arizona State University; Phoenix AZ, USA.

²²Department of Geosciences, University of Fribourg; Fribourg, Switzerland.

²³IFP Energies Nouvelles; Paris, France.

²⁴School of the Environment, The University of Queensland; St. Lucia QLD, Australia.

²⁵Key Laboratory of Polar Ecosystem and Climate Change, Ministry of Education; and School of Oceanography, Shanghai Jiao Tong University, Shanghai 200030, China.

²⁶Global Undersea Research Unit, University of Alaska Fairbanks; Moss Landing CA, USA.

²⁷Arctic Research Support and Logistics; Washington DC, USA.

²⁸Department of Communication, University of North Dakota and Blue Marble Space
Institute of Science, USA

*Corresponding author. Email: LissenbergCJ@cardiff.ac.uk

5

Abstract:

The upper mantle is critical for our understanding of terrestrial magmatism, crust formation, and element cycling between Earth's solid interior, hydrosphere, atmosphere, and biosphere. Mantle composition and evolution has been primarily inferred via surface sampling and indirect methods. We recovered a long (1268 m) section of serpentinized abyssal mantle peridotite, interleaved with thin gabbroic intrusions. We find depleted compositions, with significant variations in mantle mineralogy controlled by melt flow. Dunite zones have predominantly intermediate dips, in contrast to the originally steep mantle fabrics, indicative of oblique melt transport. Extensive hydrothermal fluid-rock interaction is recorded across the full depth of the core and is overprinted by oxidation in the upper 200 m. Alteration patterns are consistent with vent fluid composition in the nearby Lost City hydrothermal field.

Main Text:

Introduction

The upper mantle is a fundamental part of the Earth system. Melt extraction from the convecting portion of the mantle (the asthenosphere) over Earth's history has led to depletion of incompatible (magmaphile) elements and the formation of crust. In turn, the ocean crust and lithospheric mantle is recycled back into the deep Earth at subduction zones. Together, these processes exert strong controls upon planetary-scale chemical cycling between the mantle, lithosphere, oceans, and biosphere for a range of elements and compounds, including water (1) and carbon (2). Furthermore, exposure of mantle rocks to seawater produces dynamic hydrothermal systems where the primary minerals in mantle peridotite are altered to secondary minerals, including serpentine and magnetite, thereby releasing molecular hydrogen (H_2 ; (3, 4)). This H_2 can further fuel the generation of organic molecules in the absence of life including organic acids, short-chain hydrocarbons, and methane (5). Hence, peridotite-hosted hydrothermal systems have been proposed as models of settings where prebiotic chemistry may have led to the development of life on early Earth and other planetary bodies (6).

Studying mantle evolution and associated hydrothermal processes is challenging due to limited accessibility as the mantle is normally covered by crust. Mantle sections of ophiolites are an exception, but reflect subduction-related igneous processes (7) and may be overprinted during and/or after emplacement (8). Abyssal peridotites, exposed locally by tectonic processes along slow- and ultraslow-spreading mid-ocean ridges and transform faults, have yielded important insights into mantle composition, melting and serpentinization (9-11), but the vast majority of these rocks have been obtained by dredging. Hence, they lack the context, spatial continuity, and orientation information critical for understanding a range of processes, including the spatial scale of compositional variations, melt migration, mantle flow, and hydrothermal alteration. Further, these rocks are overprinted by seafloor weathering, providing a challenge to reconstructing serpentinization processes (12). Only drilling of abyssal peridotite provides a continuous and oriented record of the upper mantle. However, this sort of drilling has proved challenging, with the deepest hole reaching only 200.8 meters below the seafloor (mbsf) with limited recovery of drill core (47%) (13).

Drilling a mantle peridotite section at Atlantis Massif

We recovered a 1268 m long section of serpentinized oceanic mantle peridotite, interleaved with thin gabbroic intrusions, from Atlantis Massif (30°N, Mid-Atlantic Ridge) (fig. S1). The Atlantis Massif is an oceanic core complex capped by a domal oceanic detachment fault that was active between ~0.4-2 Ma (14, 15). Along the south wall of the massif, detachment faulting exhumed serpentinized mantle rocks with minor gabbroic intrusions (16) (fig. S2). The intersection of mantle rocks, serpentinization, abiotic organic synthesis, and seafloor life is epitomized at Atlantis Massif by the Lost City hydrothermal field (17), which vents warm (40–115°C), alkaline fluids rich in H_2 and abiotically synthesized formate, short-chain hydrocarbons, and methane (CH_4), and supports abundant life (18-22).

International Ocean Discovery Program (IODP) Expedition 399 (April-June 2023) targeted Site U1601, 800 m north of the Lost City field (fig. S1). A 55 m deep pilot hole (U1601A) was drilled, followed by a 1268 m deep hole (U1601C), recovering predominantly serpentinized mantle peridotites with subordinate gabbro (fig. 1A). The depth of U1601C far exceeds previous efforts to drill oceanic mantle rocks (fig. S3). Overall recovery was 71%, including long intervals of variably serpentinized harzburgite with close to 100% recovery.

The nearly continuous recovery provides an opportunity to obtain a robust and quantitative lithological, mineralogical, structural, and alteration inventory of the upper mantle.

Furthermore, the oriented nature of the section provides constraints on the geometry of mantle upwelling and melt flow. Because the detachment fault roots into and crosses the current Mid-Atlantic Ridge axis (15), it captures the central upwelling zone beneath the ridge axis. We can therefore trace the section from the melting zone, through zones of melt transport, to gabbro intrusion in the lithosphere and finally alteration. This provides an unequalled framework for understanding the composition of the upper mantle, the processes of partial melting, melt migration, and hydrothermal alteration, and hence the processes that control the flux of heat and mass between the upper mantle, lithosphere, biosphere, and oceans.

Mantle composition and structure: melt migration controls

Serpentinized peridotite constitutes 68% of the rock types recovered from Hole U1601C, and includes harzburgite (82%), orthopyroxene (opx) bearing dunite (1%-10% opx; 13%) and dunite (<1% opx; 5%) (fig. 1A, S4) (table S1). Lherzolite was observed in one thin section; plagioclase peridotites were not observed away from immediate contacts with gabbro. The different types of peridotite alternate at various scales and frequencies (fig. 1A), and are depleted, with modal clinopyroxene in harzburgite averaging 1.0% (fig. 2A, S5) (table S2); many samples lack clinopyroxene altogether. These mineralogical observations are consistent with preliminary whole-rock geochemical data (table S3), which show that Site U1601 peridotites have high MgO/SiO₂ and low Al₂O₃/SiO₂, falling on the depleted end of the array defined by global mantle rocks (fig. 2B). Near-surface samples previously obtained from Atlantis Massif are similarly depleted, recording degrees of melting of up to ~20% (23); critically, however, the Site U1601 peridotites define tight MgO/SiO₂-Al₂O₃/SiO₂ correlation and fall closer to the mantle array, indicating that they retained their primary mantle compositions to a greater degree.

Harzburgite has average modal proportions of 15.9% opx (fig. 1B,C) (table S4), lower than expected for proposed oceanic mantle, which retains >20% opx even after extensive partial melting (11, 24). Further, opx abundance varies significantly on scales ranging from the centimeter to hundreds of meters, forming a continuum from 0-30% (fig. 1B,C). Dunite occurs as zones in harzburgite and, more frequently, in opx-bearing dunite. These zones are distributed throughout U1601C, but are concentrated particularly in the upper 200 mbsf and around 800 mbsf (fig. 1A), and are typically tens of centimeters thick. The thickest interval of harzburgite without zones of (opx-bearing) dunite (though with some gabbroic intervals) is 22 m (359-381mbsf). Contacts between dunite and the surrounding peridotites are nearly always gradational, with opx proportions decreasing over centimeters to decimeters. Well-defined dunite zones (fig. 3C) are an endmember of a continuum of variations in opx content in the mantle rocks, with the full spectrum of harzburgite to dunite preserved in the core (fig. 3A-C).

We posit that the observed variations in mineralogy and therefore lithology are controlled by melt migration and the associated dissolution of opx and precipitation of olivine (25, 26), superimposed on the residues of relatively high degrees of melting. We find a broad correlation between opx abundance and grain size, with smaller grain size (generally 2-5 mm) in opx-bearing dunite compared to the most opx-rich harzburgites (5-8 mm; fig. S6). It follows that the proportion and grain size of opx in the section is controlled largely by dissolution from migrating melts, with the proportion of opx inversely proportional to the integrated flux of reactive melt. Additional evidence for melt migration is the common occurrence of Cr-spinel with vermicular habit, the commonly interstitial habits of clinopyroxene and some of the opx, and the occurrence of rare (0.1%; fig. S4) ultramafic veins (wehrlite, orthopyroxenite, (olivine) websterite). We conclude that the relatively low overall opx proportions, and variations in peridotite mineralogy from the hundred-meter scale

down to the centimeter scale, reflect melt migration with melt flux varying on a range of scales.

The geometry of melt flow is captured by the orientation of the dunite zones. Harzburgite-dunite contacts have variable orientations, with a mode of 40° (fig. 1H,I) (table S5). The dip distribution of these contacts differs from the modeled distribution of randomly oriented 2D structures (fig. 1H), indicating that both the predominance of intermediate dips and the scarcity of shallow dips is geologically significant. This contrasts with mantle fabrics (fig. 1D,E, S7), which typically have a subhorizontal to moderately inclined dip in the core (mode 0° ; fig. 1F,G) (table S6). Exhumation of Atlantis Massif and our recovered core section was accommodated by fault-block rotation around a subhorizontal ridge-parallel axis. Paleomagnetic data record $46 \pm 6^\circ$ rotation below temperatures of 580°C (27), but the total magnitude of rotation in the lithosphere, based on initial fault dips at other oceanic core complexes, is estimated to be at least $60\text{--}70^\circ$ (28, 29). If asthenospheric upwelling was vertical (30, 31), we would expect a further rotation of $20\text{--}30^\circ$. Although internal deformation during exhumation in both the asthenosphere and lithosphere will have affected the orientation of the section, we are confident that the original plunge of the drill hole was low ($<30^\circ$), and essentially across the upwelling zone. These constraints imply that the low dip of the mantle fabrics translates to predominantly steep initial dips prior to rotation, consistent with an origin by ductile flow during upwelling (fig. 4A,B). The measured $\sim 40^\circ$ discordance between the mantle fabrics and dunite contacts across the full depth of Hole U1601C (fig. 1I) is difficult to reconcile with models where melt migrates vertically before travelling along the base of the lithosphere in a narrow (200-300 m) zone (32). Instead, it is consistent with the formation of a network of dunite channels with variable but predominantly intermediate dips oblique to mantle upwelling as a result of melt focusing toward the ridge axis (fig. 4C) (33, 34).

Gabbroic bodies and veins comprise 31% of the recovered core from Hole U1601C (table S1) and are concentrated towards the bottom (>950 mbsf; fig. 1A). Gabbroic rocks generally have sutured contacts with host peridotites, indicative of emplacement into relatively warm lithospheric mantle. Lithologically, the gabbroic rocks are dominated by gabbro, with lesser gabbro-norite and olivine gabbro (fig. S4). Other gabbroic rock types (e.g., troctolite, oxide gabbro) are rare ($<3\%$). The size distribution of gabbroic intrusions shows that a substantial majority (80%) of the 265 units logged occur as veins <1 m thick, with many of millimeter to centimeter thickness, with progressively fewer intrusions at the 1-10 meter and >10 m scales (fig. S8) (table S7). The dips of these gabbroic intrusions are highly variable, though steep dips predominate and shallow dips are relatively rare (fig. S9) (table S8). Together, the predominance of small intrusion size coupled with highly variable orientation indicate that the gabbroic intrusions comprise a net vein complex (fig 4A,D).

Lithologies, alteration patterns consistent with predictions of Lost City host rocks

The deep penetration on Expedition 399 allows for a reconstruction of hydrothermal alteration histories below the zone of seafloor weathering. Furthermore, the Site U1601 peridotites are potentially representative of different zones of the Lost City circulation pathway, including its deepest stockworks. This is important, because Lost City is an exemplar of an ultramafic-hosted, alkaline seafloor vent, a modern analog of the environment in which some theories propose life first emerged on early Earth (6, 19-22). The peridotite we recovered is generally highly serpentinized, from $\sim 40\%$ in the least altered peridotite to 100% in fully serpentinized peridotite (fig. 1J, 3D-F, S10, S11). We calculated average extents of serpentinization of 80% and 90% from a linear regression of discrete grain density measurements (table S9) and microscopic observations (table S10), respectively (fig. 1J). A systematic increase or decrease in extent of serpentinization downhole is not evident from

current density data or microscopic observations (fig. 1J). Instead, substantial variations occur on the centimeter to decameter scale. However, mafic lithologies exert a strong influence on the extent of alteration. Our observations suggest that serpentinization is a complex and protracted multistage process covering a wide range of environmental and chemical conditions throughout the borehole. Opx is partially to completely altered to serpentine with local co-occurrence of talc, chlorite, and amphibole in bastite texture (fig. S10), consistent with initially high alteration temperatures above 350-400°C (35). Olivine is highly altered to serpentine and magnetite and forms a mesh texture dominated by lizardite, minor chrysotile, and brucite that is partly replaced by iowaite (fig. 3E). The serpentine-magnetite mesh texture is cut by different vein types: earlier generations are dominated by lizardite and magnetite and later veins are composed of chrysotile, suggesting that several serpentinization events occurred (fig. 3F, S10). The abundance of magnetite in mesh texture implies H₂ formation and strongly reducing conditions (36). Previous work on shallow boreholes (<16.5 mbsf) and surficial sampling documented two stages of hydration and serpentinization, an initial stage at temperatures above 350-400°C that alters opx to talc and tremolite but preserves olivine, followed by pervasive serpentinization at temperatures <350°C (37, 38). Our findings are generally consistent with this model, suggesting that episodic serpentinization extends to the full depth of the section and hence may capture the hydrothermal processes operating in the stockwork zone beneath Lost City.

Equivalent to alteration conditions recorded in serpentinite, mineral associations, and vein types in gabbroic intrusions suggest a continuous decrease in the alteration temperatures from amphibolite to (sub-) greenschist facies conditions (fig. S13). Recovered gabbroic rocks range from fresh to completely altered, with more extensive alteration in intervals with a high degree of ductile and/or brittle deformation, a high density of hydrothermal veins, and at contacts with serpentinized peridotite. Olivine in gabbro is altered to serpentine, magnetite, talc, and sulfides in mesh texture, whereas clinopyroxene is altered to amphibole, talc, and chlorite. Igneous plagioclase is replaced by secondary (hydrothermal) plagioclase, chlorite, prehnite, and zeolite. The main types of veins include amphibole, chlorite, talc, carbonate, and zeolite.

In the upper ~200 m of Hole 1601C, serpentinite shows evidence for a local low-temperature overprint (fig. S14); this overprint was rarely observed below this level. There, magnetite formed during serpentinization is oxidized to iron oxide and iron oxyhydroxide minerals while brucite is altered to iowaite. Continuing low-temperature alteration can result in the formation of clay minerals. Elevated natural gamma radiation counts indicate enrichments of radiogenic elements, including U, K, and Th (fig. 1K, S15) (table S11). The higher abundances of uranium in the upper ~200 mbsf (table S11) reflect its heterogeneous uptake into serpentinized peridotite during interaction with seawater near the seafloor (38-40). Such low temperature interaction may cause dissolution of brucite, olivine, and in extreme cases serpentine, leading to high rock porosity and removal of Mg, with simultaneous uptake of seawater sulfur, carbon, and uranium into the rocks, to extents that are potentially significant for global ocean fluxes (12, 41-44). This is consistent with both serpentine and whole-rock compositions of shallow samples recovered during IODP Expedition 357 (23, 38), including their elevated uranium and scatter in Mg-Si-Al relationships (fig. 2B); in contrast, our current data from Site U1601 show little evidence for mass exchange of Mg and Si during serpentinization (fig. 2B).

Carbonate veins are found throughout the hole (fig. 1A). Such veins may be formed from both seawater carbon and mantle-derived volatiles over a range of temperatures (45). In the peridotite-dominated section below the zone of low temperature seawater alteration (~200 – 950 mbsf), carbonate veins predominantly occur in serpentinized peridotites in association with thin (<1 mm wide) subparallel and fibrous chrysotile veins, while minor carbonates also

occur in the serpentinite groundmass without apparent association with serpentine veins (fig. S16). From U1601A microscopic observations (fig. 3F), some carbonate veins reopen former chrysotile veins suggesting that carbonation took place at the end of or subsequent to serpentinitization. This suggests that the chrysotile veins that formed with exhumation were also closely linked to carbonation either contemporaneously or because CO₂-rich fluids preferentially followed these serpentine veins. Carbonate veins decrease in abundance in the lower part of the Hole (fig. 1A), but locally intense carbonation and veining is seen associated with highly altered gabbros (Fig. S16), including apparent replacement of silicate minerals by carbonate. A decrease in the amount of carbonate within serpentinite away from altered gabbro suggests Ca is derived from gabbro alteration (Fig. S16). Further, massive (mm to cm thick) carbonate-talc veins are hosted in the serpentinitized peridotites in close association with the gabbroic intrusions that themselves host carbonate-prehnite veins. The magmatic veins may provide the requisite conditions for carbonate precipitation by facilitating fluid flow pathways at the contact with peridotite (38) and/or through the delivery of mantle-derived volatiles (45).

The primary lithologies and subsequent alteration reactions we documented (fig. 4E) match predictions of the thermal and mineralogical controls on Lost City fluid geochemistry. Downwelling seawater deposits uranium onto the shallowest rocks (<200 mbsf; fig. 1K) (23), leading to near-zero U concentrations (<0.2 ppb) in the fluids compared to average seawater (3 ppb) (46). Fluid pH and major ion compositions reflect serpentinitization of peridotite at 180-200°C (19, 22, 47-49), while elevated concentrations of Rb and Cs, well above values expected for equilibration with serpentinite, are interpreted to reflect gabbroic inputs (22). The shallow boreholes drilled during IODP Expedition 357 contain rare gabbroic intrusions into host peridotite that facilitate fluid flow and lead to exchange of silica, sulfur, and metals between the harzburgite and gabbro (38). We found the relationship between gabbroic intrusions and hydrothermal alteration to be common throughout the harzburgite-dominated sections of Hole U1601C. Hence, our data support the idea that Lost City fluids reflect interactions with both ultramafic and mafic rocks in its plumbing system, similar to the relationship of hydrothermally altered rocks recovered from Site U1601.

New insights into the depleted mantle

Above, we have shown that the recovery of a long section of serpentinitized peridotites and associated gabbros has provided a comprehensive lithological, mineralogical and structural inventory of the oceanic upper mantle. We have documented, for the first time, the spatial scale of mineralogical variation in the upper mantle, and found substantial variations on the centimeter to hundreds of meters scale. Overall, the pyroxene content of the peridotite is unexpectedly low, which may result from both high degrees of depletion and pyroxene dissolution during melt flow. Contrary to often-invoked models, focused melt migration was oblique to mantle upwelling. Whole-rock compositions reinforce the depleted nature of the section and show that the U1601C drill core preserves primary compositions better than seafloor samples, despite the generally high degrees of serpentinitization. Surprisingly, serpentinitization shows no decrease downhole, remaining advanced throughout; instead, large variations in extent of serpentinitization occur on the centimeter to decameter scale. The depth to which oxidative weathering occurs was shown to be ~200 m. Hydrothermal alteration was facilitated by gabbroic intrusions, supporting their unexpected role in regulating the composition of fluids from peridotite-hosted hydrothermal vents.

The comprehensive rock record obtained during Expedition 399 provides a wealth of opportunities to make fundamental advances on our understanding of the oceanic upper mantle. These opportunities include a determination of mantle heterogeneity on the centimeter to kilometer scale, which is difficult to resolve in the mid-ocean ridge basalt

record that is conventionally used for reconstructing mantle heterogeneity. Further, the depleted nature of the section provides an opportunity to investigate the role of previous depletion in governing mantle composition and melting. The continuous nature of the core, and its re-orientation, will also be instrumental in studies of spatial variations in melting and melt transport, as well as research into mantle flow and the associated deformation mechanisms. The recovery of variably serpentinized rocks from beyond the zone of oxidation offers an opportunity to reconstruct H₂ production during serpentinization and its role in fueling microbial activity, as well as its mass exchange during hydrothermal alteration at a range of temperatures and its impact on global geochemical cycles. Finally, the penetration of Hole U1601C into the subsurface of the Lost City hydrothermal field provides an opportunity to study the limits and extent of life in the oceanic lithosphere and a potential platform for future experiments on the geology, chemistry, and biology of an off-axis hydrothermal system.

References

1. J. Korenaga, N. J. Planavsky, D. A. Evans, Global water cycle and the coevolution of the Earth's interior and surface environment. *Philosophical Transactions of the Royal Society A: Mathematical, Physical and Engineering Sciences* **375**, 20150393 (2017).
2. R. Dasgupta, M. M. Hirschmann, The deep carbon cycle and melting in Earth's interior. *Earth and Planetary Science Letters* **298**, 1-13 (2010).
3. J. L. Charlou *et al.*, High production and fluxes of H₂ and CH₄ and evidence of abiotic hydrocarbon synthesis by serpentinization in ultramafic-hosted hydrothermal systems on the Mid-Atlantic Ridge. *Washington DC American Geophysical Union Geophysical Monograph Series* **188**, 265-296 (2010).
4. C. Neal, G. Stanger, Hydrogen generation from mantle source rocks in Oman. *Earth and Planetary Science Letters* **66**, 315-320 (1983).
5. T. M. McCollom, J. S. Seewald, Abiotic synthesis of organic compounds in deep-sea hydrothermal environments. *Chemical reviews* **107**, 382-401 (2007).
6. W. Martin, J. Baross, D. Kelley, M. J. Russell, Hydrothermal vents and the origin of life. *Nature Reviews Microbiology* **6**, 805-814 (2008).
7. B.-X. Su *et al.*, Mantle peridotites of ophiolites rarely preserve reliable records of paleo-oceanic lithospheric mantle. *Earth-Science Reviews*, 104544 (2023).
8. E. S. Falk, P. B. Kelemen, Geochemistry and petrology of listvenite in the Samail ophiolite, Sultanate of Oman: Complete carbonation of peridotite during ophiolite emplacement. *Geochimica et Cosmochimica Acta* **160**, 70-90 (2015).
9. H. J. B. Dick, in *Magmatism in the Ocean Basins*, Geological Society Special Publication No. 42, A. D. Saunders, M. J. Norry, Eds. (1989), pp. 71-105.
10. M. O. Schrenk, W. J. Brazelton, S. Q. Lang, Serpentinization, carbon, and deep life. *Reviews in Mineralogy and Geochemistry* **75**, 575-606 (2013).
11. J. M. Warren, Global variations in abyssal peridotite compositions. *Lithos* **248**, 193-219 (2016).
12. F. Klein, S. Humphris, W. Bach, Brucite formation and dissolution in oceanic serpentinite. *Geochemical Perspectives Letters* **16**, 1-5 (2020).
13. M. Cannat, J. A. Karson, D. J. Miller, *et al.*, Eds., (Ocean Drilling Program, College Station, TX, 1995), vol. 153, pp. 798.
14. D. K. Blackman *et al.*, Drilling constraints on lithospheric accretion and evolution at Atlantis Massif, Mid-Atlantic Ridge 30°N. *Journal of Geophysical Research: Solid Earth* **116**, B07103 (2011).
15. J. Escartín *et al.*, Tectonic termination of oceanic detachment faults, with constraints on tectonic uplift and mass wasting related erosion rates. *Earth and Planetary Science Letters* **584**, 117449 (2022).

16. J. Karson *et al.*, Detachment shear zone of the Atlantis Massif core complex, Mid-Atlantic Ridge, 30° N. *Geochemistry, Geophysics, Geosystems* **7**, (2006).
17. D. S. Kelley *et al.*, An off-axis hydrothermal vent field near the Mid-Atlantic Ridge at 30° N. *Nature* **412**, 145-149 (2001).
- 5 18. W. J. Brazelton, M. O. Schrenk, D. S. Kelley, J. A. Baross, Methane- and Sulfur-Metabolizing Microbial Communities Dominate the Lost City Hydrothermal Field Ecosystem. *Applied and Environmental Microbiology* **72**, 6257-6270 (2006).
19. D. S. Kelley *et al.*, A serpentinite-hosted ecosystem: the Lost City hydrothermal field. *Science* **307**, 1428-1434 (2005).
- 10 20. S. Q. Lang, D. A. Butterfield, M. Schulte, D. S. Kelley, M. D. Lilley, Elevated concentrations of formate, acetate and dissolved organic carbon found at the Lost City hydrothermal field. *Geochimica et Cosmochimica Acta* **74**, 941-952 (2010).
21. G. Proskurowski, M. D. Lilley, D. S. Kelley, E. J. Olson, Low temperature volatile production at the Lost City Hydrothermal Field, evidence from a hydrogen stable isotope geothermometer. *Chemical Geology* **229**, 331-343 (2006).
- 15 22. W. Seyfried Jr, N. J. Pester, B. M. Tutolo, K. Ding, The Lost City hydrothermal system: Constraints imposed by vent fluid chemistry and reaction path models on seafloor heat and mass transfer processes. *Geochimica et Cosmochimica Acta* **163**, 59-79 (2015).
- 20 23. S. A. Whattam *et al.*, Geochemistry of serpentinized and multiphase altered Atlantis Massif peridotites (IODP Expedition 357): Petrogenesis and discrimination of melt-rock vs. fluid-rock processes. *Chemical Geology* **594**, 120681 (2022).
24. Y. Niu, Mantle Melting and Melt Extraction Processes beneath Ocean Ridges: Evidence from Abyssal Peridotites. *Journal of Petrology* **38**, 1047-1074 (1997).
- 25 25. P. B. Kelemen, N. Shimizu, V. J. M. Salters, Extraction of mid-ocean-ridge basalt from the upwelling mantle by focused flow of melt in dunite channels. *Nature* **375**, 747-753 (1995).
26. Z. Morgan, Y. Liang, An experimental and numerical study of the kinetics of harzburgite reactive dissolution with applications to dunite dike formation. *Earth and Planetary Science Letters* **214**, 59-74 (2003).
- 30 27. A. Morris *et al.*, Footwall rotation in an oceanic core complex quantified using reoriented Integrated Ocean Drilling Program core samples. *Earth and Planetary Science Letters* **287**, 217-228 (2009).
28. B. J. deMartin, R. A. Sohn, J. Pablo Canales, S. E. Humphris, Kinematics and geometry of active detachment faulting beneath the Trans-Atlantic Geotraverse (TAG) hydrothermal field on the Mid-Atlantic Ridge. *Geology* **35**, 711-714 (2007).
- 35 29. C. J. MacLeod *et al.*, Life cycle of oceanic core complexes. *Earth and Planetary Science Letters* **287**, 333-344 (2009).
30. L. G. Montési, M. D. Behn, Mantle flow and melting underneath oblique and ultraslow mid-ocean ridges. *Geophysical Research Letters* **34**, (2007).
- 40 31. J.-A. Olive, in *Dynamics of plate tectonics and mantle convection*. (Elsevier, 2023), pp. 483-510.
32. D. W. Sparks, E. M. Parmentier, Melt extraction from the mantle beneath spreading centers. *Earth and Planetary Science Letters* **105**, 368-377 (1991).
- 45 33. R. F. Katz, S. M. Weatherley, Consequences of mantle heterogeneity for melt extraction at mid-ocean ridges. *Earth and Planetary Science Letters* **335-336**, 226-237 (2012).
34. P. B. Kelemen, M. Braun, G. Hirth, Spatial distribution of melt conduits in the mantle beneath oceanic spreading ridges: Observations from the Ingalls and Oman ophiolites. *Geochemistry, Geophysics, Geosystems* **1**, (2000).
- 50

35. D. E. Allen, W. Seyfried Jr, Compositional controls on vent fluids from ultramafic-hosted hydrothermal systems at mid-ocean ridges: An experimental study at 400 C, 500 bars. *Geochimica et Cosmochimica Acta* **67**, 1531-1542 (2003).
36. F. Klein *et al.*, Magnetite in seafloor serpentinite—Some like it hot. *Geology* **42**, 135-138 (2014).
37. C. Boschi, A. Dini, G. L. Früh-Green, D. S. Kelley, Isotopic and element exchange during serpentinization and metasomatism at the Atlantis Massif (MAR 30 N): insights from B and Sr isotope data. *Geochimica et Cosmochimica Acta* **72**, 1801-1823 (2008).
38. S. Rouméjon, G. L. Früh-Green, B. N. Orcutt, I. E. S. Party, Alteration heterogeneities in peridotites exhumed on the southern wall of the Atlantis Massif (IODP Expedition 357). *Journal of Petrology* **59**, 1329-1358 (2018).
39. J. Kodolányi, T. Pettke, C. Spandler, B. S. Kamber, K. Gméling, Geochemistry of ocean floor and fore-arc serpentinites: constraints on the ultramafic input to subduction zones. *Journal of Petrology* **53**, 235-270 (2012).
40. M. Seitz, S. Hart, Uranium and boron distributions in some oceanic ultramafic rocks. *Earth and Planetary Science Letters* **21**, 97-107 (1973).
41. J. C. Alt *et al.*, The role of serpentinites in cycling of carbon and sulfur: Seafloor serpentinization and subduction metamorphism. *Lithos* **178**, 40-54 (2013).
42. S. Pujatti, O. Plümper, B. M. Tutolo, Weathering-driven porosity generation in altered oceanic peridotites. *Earth and Planetary Science Letters* **604**, 118006 (2023).
43. E. M. Schwarzenbach, G. L. Früh-Green, S. M. Bernasconi, J. C. Alt, A. Plas, Serpentinization and carbon sequestration: A study of two ancient peridotite-hosted hydrothermal systems. *Chemical Geology* **351**, 115-133 (2013).
44. J. E. Snow, H. J. B. Dick, Pervasive magnesium loss by marine weathering of peridotite. *Geochimica et Cosmochimica Acta* **59**, 4219-4235 (1995).
45. L. Ternieten, G. L. Früh-Green, S. M. Bernasconi, Distribution and sources of carbon in serpentinized mantle peridotites at the Atlantis Massif (IODP Expedition 357). *Journal of Geophysical Research: Solid Earth* **126**, e2021JB021973 (2021).
46. K. A. Ludwig, D. S. Kelley, D. A. Butterfield, B. K. Nelson, G. Früh-Green, Formation and evolution of carbonate chimneys at the Lost City Hydrothermal Field. *Geochimica et cosmochimica acta* **70**, 3625-3645 (2006).
47. D. E. Allen, W. Seyfried Jr, Serpentinization and heat generation: constraints from Lost City and Rainbow hydrothermal systems. *Geochimica et Cosmochimica Acta* **68**, 1347-1354 (2004).
48. S. Q. Lang *et al.*, Microbial utilization of abiogenic carbon and hydrogen in a serpentinite-hosted system. *Geochimica et Cosmochimica Acta* **92**, 82-99 (2012).
49. J. L. Palandri, M. H. Reed, Geochemical models of metasomatism in ultramafic systems: serpentinization, rodingitization, and sea floor carbonate chimney precipitation. *Geochimica et Cosmochimica Acta* **68**, 1115-1133 (2004).
50. S. J. Martel, Analysis of fracture orientation data from boreholes. *Environmental & Engineering Geoscience*, 213-233 (1999).
51. M. Godard *et al.*, Geochemistry of a long in-situ section of intrusive slow-spread oceanic lithosphere: Results from IODP Site U1309 (Atlantis Massif, 30°N Mid-Atlantic-Ridge). *Earth and Planetary Science Letters* **279**, 110-122 (2009).
52. R. K. Workman, S. R. Hart, Major and trace element composition of the depleted MORB mantle (DMM). *Earth and Planetary Science Letters* **231**, 53-72 (2005).
53. E. Jagoutz *et al.*, in *In: Lunar and Planetary Science Conference, 10th, Houston, Tex., March 19-23, 1979, Proceedings. Volume 2.(A80-23617 08-91) New York, Pergamon Press, Inc., 1979, p. 2031-2050. Research supported by the Deutsche Forschungsgemeinschaft.* (1979), vol. 10, pp. 2031-2050.

54. S. R. Hart, A. Zindler, In search of a bulk-earth composition. *Chemical Geology* **57**, 247-267 (1986).
55. W. F. McDonough, S.-s. Sun, The composition of the Earth. *Chemical Geology* **120**, 223-253 (1995).
56. J. F. Casey, in *Proc. ODP, Sci. Res.*, J. A. Karson, M. Cannat, D. J. Miller, D. Elthon, Eds. (Ocean Drilling Program, College Station, TX, 1997), vol. 153, pp. 181-241.
57. M. Godard, Y. Lagabriele, O. Alard, J. Harvey, Geochemistry of the highly depleted peridotites drilled at ODP Sites 1272 and 1274 (Fifteen-Twenty Fracture Zone, Mid-Atlantic Ridge): Implications for mantle dynamics beneath a slow spreading ridge. *Earth and Planetary Science Letters* **267**, 410-425 (2008).
58. H. Paulick *et al.*, Geochemistry of abyssal peridotites (Mid-Atlantic Ridge, 15° 20' N, ODP Leg 209): implications for fluid/rock interaction in slow spreading environments. *Chemical geology* **234**, 179-210 (2006).
59. J.-L. Bodinier, M. Godard, Orogenic, ophiolitic, and abyssal peridotites. *Treatise on geochemistry* **2**, 568 (2003).
60. C. B. Grimes, B. E. John, M. Cheadle, J. L. Wooden, Protracted construction of gabbroic crust at a slow-spreading ridge: Constraints from ²⁰⁶Pb/²³⁸U zircon ages from Atlantis Massif and IODP Hole U1309D (30°N, MAR). *Geochemistry, Geophysics, Geosystems* **9**, doi:10.1029/2008GC002063 (2008).
61. R. Coggon *et al.*, Expedition 390/393 methods. *Proceedings of the International Ocean Discovery Program Expedition reports* **390**, (2024).
62. R. Murray, D. J. Miller, K. Kryc, Analysis of major and trace elements in rocks, sediments, and interstitial waters by inductively coupled plasma–atomic emission spectrometry (ICP-AES). *ODP Technical Note* **29**, doi:10.2973/odp.tn.2929.2000 (2000).
63. P. Blum, Physical properties handbook—A guide to the shipboard measurement of physical properties of deep-sea cores. *ODP Technical note* **26**, doi:10.2973/odp.tn.2926.1997 (1997).
64. A. J. Harding, A. F. Arnulf, D. K. Blackman, Velocity structure near IODP Hole U1309D, Atlantis Massif, from waveform inversion of streamer data and borehole measurements. *Geochemistry, Geophysics, Geosystems* **17**, 1990-2014 (2016).
65. A. Henig, D. K. Blackman, A. J. Harding, J. P. Canales, G. M. Kent, Downward continued multichannel seismic refraction analysis of Atlantis Massif oceanic core complex, 30° N, Mid-Atlantic Ridge. *Geochemistry, Geophysics, Geosystems* **13**, (2012).
66. C. Boschi, G. L. Früh-Green, A. Delacour, J. A. Karson, D. S. Kelley, Mass transfer and fluid flow during detachment faulting and development of an oceanic core complex, Atlantis Massif (MAR 30 N). *Geochemistry, Geophysics, Geosystems* **7**, (2006).
67. B. Ildefonse *et al.*, in *Developments in Marine Geology*. (Elsevier, 2014), vol. 7, pp. 449-505.

Acknowledgments: We would like to thank the captain and crew of the *JOIDES Resolution* for their dedicated work in making Expedition 399 a success. IODP staff at Texas A&M University are thanked for their efforts to (re)image and (re)curate the cores, and for organizing the post-cruise core description workshop. We thank S. Martel for clarifying the distribution of 2D planes in boreholes, and Shuguang Song, Eric Hellebrand and an anonymous reviewer for their comments and suggestions for improvements to the paper.

Funding: This research used samples and data provided by the International Ocean Discovery Program (IODP). Funding for the operation and management of the scientific

drilling vessel JOIDES Resolution was provided by the U.S. National Science Foundation (NSF) award OCE – 1326927. Funding to join Expedition 399 was provided by UK Natural Environment Research Council grants NE/X019098/1 (CJL), NE/Y001737/1 (AMM), NE/Y002350/1 (AJP) and NE/Y002415/1 (IPS); NSF grant OCE-1450528 for the U.S. Science Support Program Office associated with the International Ocean Discovery Program (USSSP-IODP Subcontract # 22O(GG009393-04) (SQL, MKR, JRD, FK, BEJ, ELL, WJB, KLD, CGW, JAR, K-YL), Juan de la Cierva fellowship FJC2021-047190-I (RC) funded by the Spanish Ministerio de Ciencia e Innovación and the Agencia Estatal de Investigación (MCIN/AEI/10.13039/501100011033); IODP France (RC, OJS, MG); IFPEN Project XBT01 (OJS); ANR Institut National des Sciences de l'Univers-CNRS grant ANR-22-EXOR-0001 Origins (MG); National Natural Science Foundation of China grant 42373003 (HL); Japan Society for the Promotion of Science grant KAKENHI 23K03528 (TN), Australia New Zealand International Consortium (ANZIC) IODP (GS); IODP-China Office and Natural Science Foundation of China grant 92251303 (FW); IODP Germany (RK), J-DESC (Japan Drilling Earth Science Consortium; NA), and National Centre for Polar and Ocean Research, Ministry of Earth Sciences, Government of India (VP).

Author contributions:

Conceptualization: AMM, SQL, CJL, CGW, FK, BEJ, MG, EMS, IPS, NA

Methodology and Investigation: All authors

Visualization: K-YL, RK, KLD, MG, HL, JRD, RC, EMS, TN, FK, AMM, SQL, AJP, MKR, CJL

Funding acquisition: AMM, CGW, CJL, FK, SQL, BEJ, MG, EMS, IS, NA

Project administration: PB

Writing – original draft: CJL, SQL, AMM

Writing – review & editing: All authors

Competing interests: Authors declare that they have no competing interests.

Data and materials availability: All data are available in the main text or the supplementary materials.

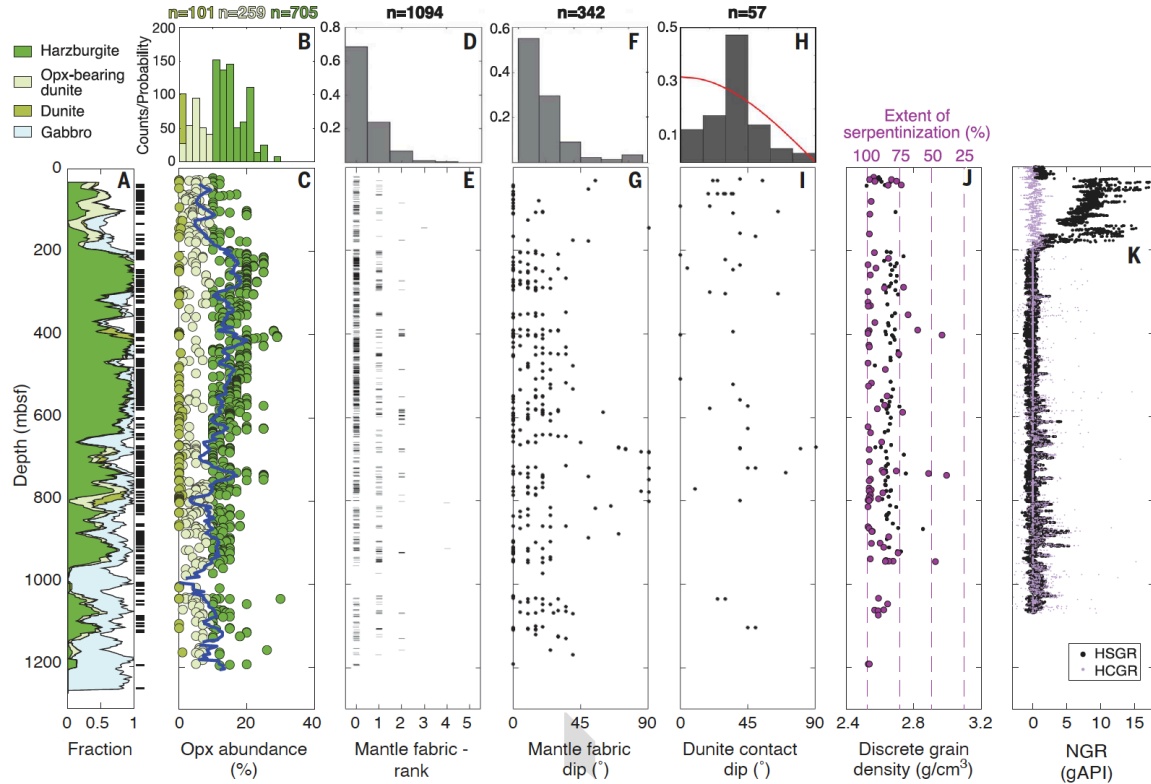


Fig 1: U1601C observations. U1601C downhole distribution of: (A) recovered rock types (20-meter running average of harzburgite, dunite (including opx-bearing dunite) and gabbro). White represents no recovery, horizontal black lines mark carbonate occurrence; (B,C) Histogram and downhole variations of modal percent opx in peridotite, with a 20-meter running average downhole (blue line) superimposed; (D,E) Histogram and downhole variations of mantle fabric intensity in peridotites (0 = protogranular; 1 = porphyroclastic (weak foliation); 2 = porphyroclastic (strong foliation); 3 = protomylonitic; 4 = mylonitic; 5 = ultramylonitic); (F,G) Histogram and downhole variations of dip of peridotite fabrics (note dip direction is not measured in drill core); (H) Histogram of dip of dunite-harzburgite contacts, along with the distribution predicted for randomly orientated planes in drill core in red (50); (I) Downhole variations of dunite-harzburgite contact dip (J) Extent of serpentinization derived from downhole shipboard density measurements of discrete peridotite samples (black) and from thin section observations (purple); (K) Wireline natural gamma ray (NGR) data including the total signal (HSGR) and the computed signal without the uranium component (HCGR).

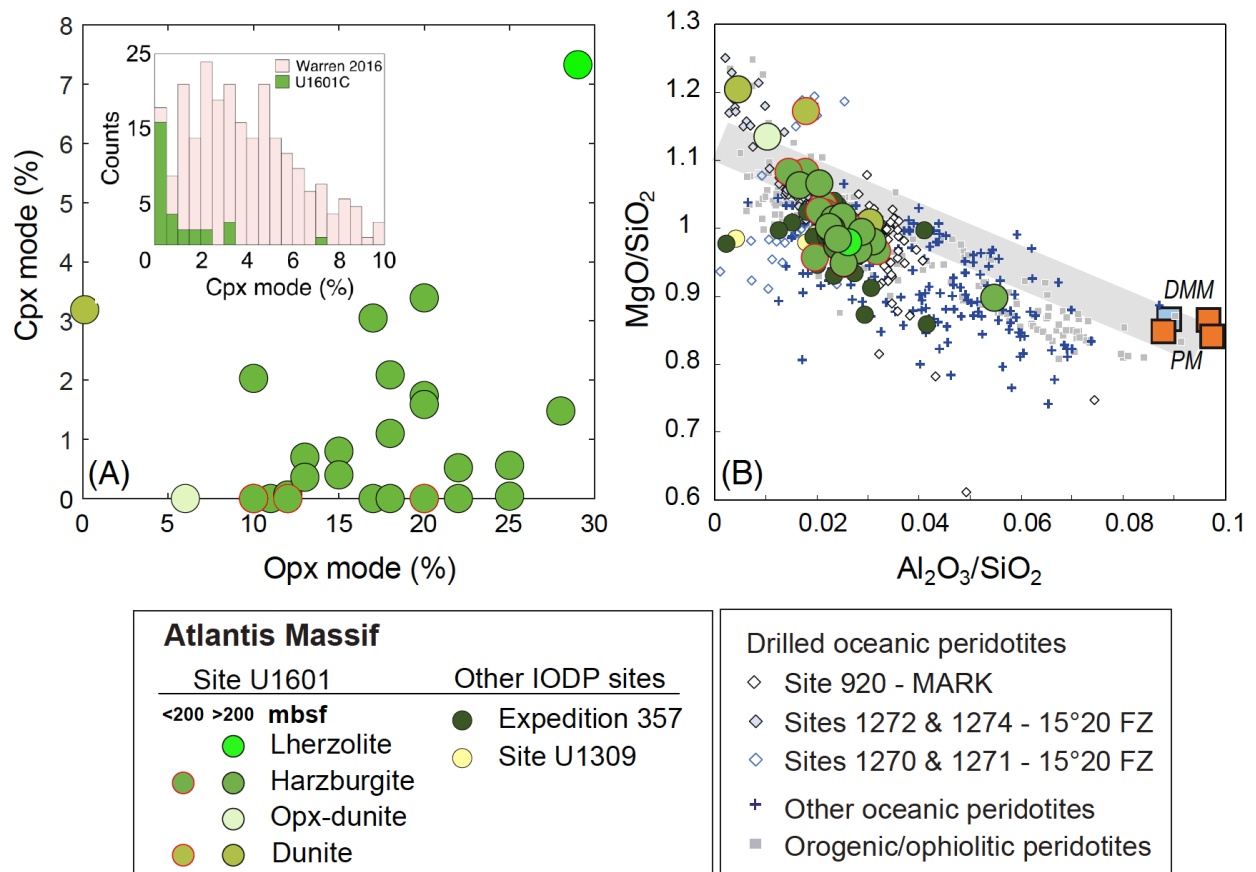


Fig 2: Mineralogy and compositions of U1601 peridotite. (A) Relationships between orthopyroxene (opx) and clinopyroxene (cpx) modal abundance. Inset shows histogram of clinopyroxene modal abundance compared with that for a compilation of abyssal peridotites (11). Orthopyroxene and clinopyroxene modal abundance is derived from macroscopic core observations and digital point counting, respectively (see methods). (B) Bulk rock compositions of peridotites sampled at IODP Site U1601 during Expedition 399 (this study) illustrated on a MgO/SiO₂ vs. Al₂O₃/SiO₂ diagram. Also shown are the compositions of peridotites and impregnated peridotites previously recovered at Atlantis Massif during IODP Expeditions 357 (23) and 304/305 (51). Composition estimates of the Depleted MORB Mantle (DMM) (52) and Primitive Mantle (PM) (53-55) are shown for comparison, together with a compilation of oceanic peridotites: Mid-Atlantic Ridge at Kane Fracture Zone (MARK) (56); Fifteen-Twenty Fracture Zone (57, 58); other oceanic peridotites together with orogenic and ophiolitic peridotites also shown for comparison (59); The thick grey line covers the different models for bulk silicate earth evolution (“terrestrial array”) (53, 54).

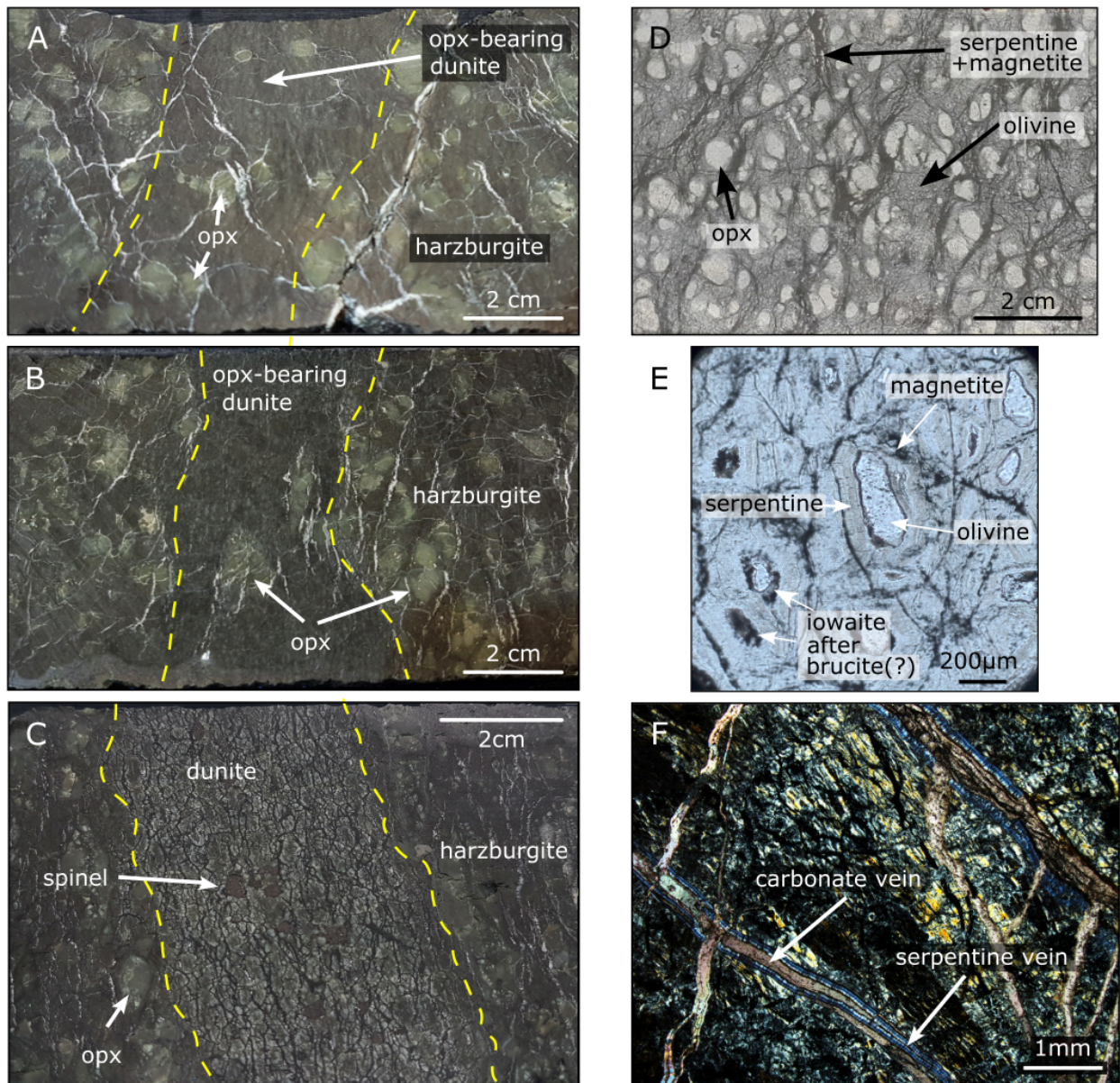


Fig 3: Core observations. Typical textures of serpentinized peridotite in core and thin section: (A-C) Progressive development of dunite from harzburgite. (A) Harzburgite with ~5 cm wide zone with lower opx content, defining a diffuse opx-bearing dunite band (Interval 399-U1601C-54R-1A, 33-45 cm). (B) ~5 cm wide band of dunite with sparse opx in harzburgite (Interval 399-U1601C-48R-2A, 14-25 cm). (C) Pure dunite band with abundant Cr-spinel in harzburgite (Interval 399-U1601C-80R-1A, 95-103 cm). (D) Relatively fresh harzburgite characterized by a partially developed mesh texture after olivine and serpentine-magnetite veins. Granular opx is mostly unaltered (Interval 399-U1601C-149R-3W, 56-67 cm). (E) Photomicrograph of mesh interiors and olivine relicts in serpentinized dunite (Interval 399-U1601A-5R-1, 124-126 cm; plane-polarized light). Typical serpentine, brucite, and iowaite mesh texture after olivine; mesh rims are composed of magnetite-serpentine veins. Presence of iowaite in sample was confirmed by XRD, location is inferred. (F) Photomicrograph of composite serpentine-carbonate vein in serpentinite (cross-polarized light). Carbonate vein crosscuts serpentinite and re-opens pre-existing serpentine vein (Interval 399-U1601A-8R-1, 38-40 cm).

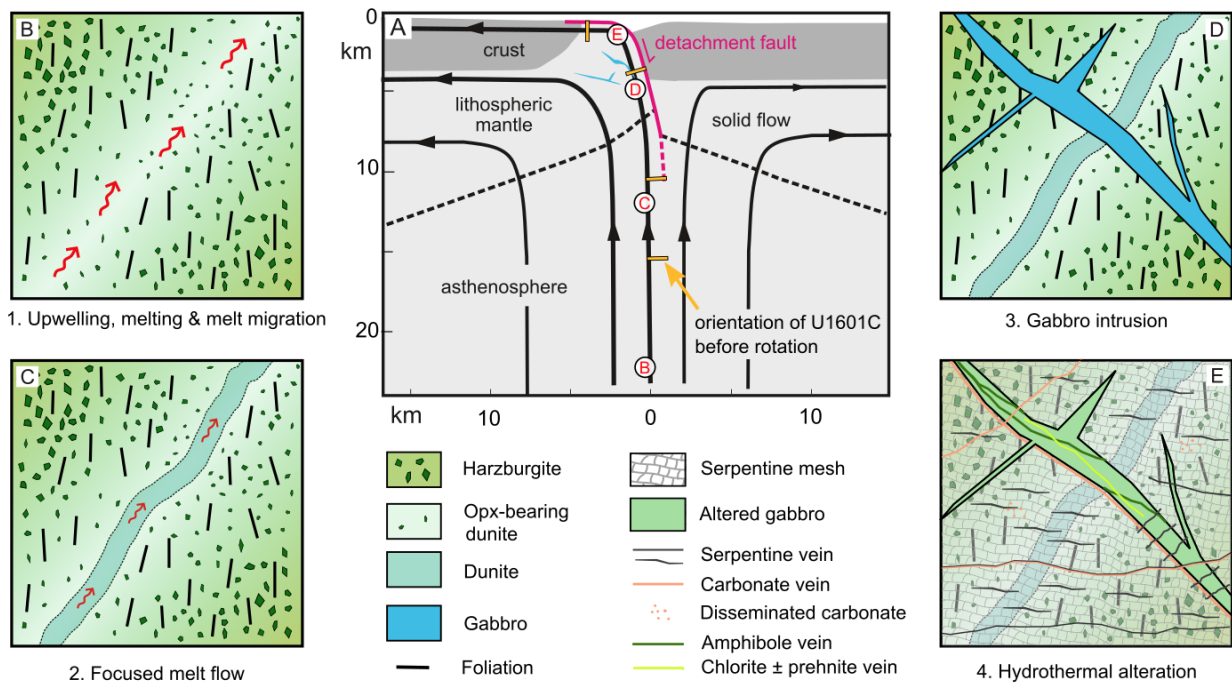


Fig. 4: Cartoons illustrating results from Hole U1601C. (A) True-scale cross-section, showing mantle upwelling, corner flow and detachment faulting. Locations of closeups (B)-(E) are indicated. Lithosphere-asthenosphere boundary from modeling of (30), for a spreading rate of 23.6 mm/yr (60). Detachment fault roots into the ridge crest (15) and captures 50-100% of the corner flow (60). Four locations of the Hole U1601C section are shown as vertical upwelling is converted to horizontal motion. Asymmetric spreading with localization of plate separation into the detachment fault leads to offsetting of the lithosphere-asthenosphere boundary and exhumation of mantle rocks to the seafloor. (B) Mantle upwelling, recorded in steep mantle fabrics, leads to partial melting and melt migration along inclined pathways, leading to the formation of opx-bearing dunites. (C) Focused melt flow leads to the formation of dunite, frequently in zones of opx-bearing dunite. (D) Melts are emplaced into the footwall of the detachment fault in the form of a net vein complex. (E) Seawater ingress during unroofing leads to hydrothermal alteration at a range of temperatures. Serpentine mesh in peridotites is crosscut by serpentine and later carbonate veins. Gabbroic rocks show early amphibole veins crosscut by chlorite±prehnite, serpentine and carbonate veins.

Materials and Methods

Rock description

Rock descriptions are based on combined core and thin section observations. Lithological units were designated on the basis of mineral proportions. For peridotite, we used the following subdivision based on orthopyroxene proportions: harzburgite ($\geq 10\%$ orthopyroxene); orthopyroxene-bearing dunite (1-10% orthopyroxene); dunite ($< 1\%$ orthopyroxene).

Orthopyroxene proportions were estimated from macroscopic observations: because of their relatively large size and uneven distribution, macroscopic estimates were considered more reliable than thin section estimates. Clinopyroxene and Cr-spinel proportions were also estimated macroscopically, and olivine proportions were then calculated by subtraction. Due to low abundance, macroscopic estimates of clinopyroxene proportions are subject to uncertainty. To obtain a more robust estimate of clinopyroxene proportions, 'digital point counting' was performed on thirty thin sections. These thin sections were selected to be representative of the peridotites in Hole U1601C and were taken away from gabbroic intervals; they are closely associated with the samples selected for geochemical analyses (see below). Digital point counting comprised two steps: first, all clinopyroxene in thin sections was traced digitally on thin section scans. The resulting line drawings were then subject to image analysis to determine clinopyroxene proportions.

The extent of serpentinization is based on thin section observations of harzburgites, orthopyroxene-bearing dunites, and dunites. No thin sections were included that cross a contact with gabbros, magmatic veins or dikes. Modal abundances of each individual mineral and the extent of alteration for each mineral individually were estimated based on thin section observations. The total extent of serpentinization was then calculated using mass balance calculations using the estimated modal abundances of olivine, orthopyroxene and clinopyroxene and the extents of alteration of olivine, orthopyroxene and clinopyroxene.

The presence of carbonates in U1601C cores was determined in a collaborative fashion during shipboard description based on macroscopic observations. Systematic tests with hydrochloric acid (HCl) were performed throughout the borehole. With the exception of massive carbonate veins, carbonates were generally too small to be observed with a hand lens and are therefore inferred by reaction with acid. The carbonate mineralogy can only be confirmed in those locations where thin sections or X-ray diffraction analyses (XRD) are currently available. As Mg-carbonates (e.g., dolomite and magnesite) do not react to HCl, their presence or absence is not included in the carbonate distributions. As a consequence, the downhole carbonate estimation might be underestimated. Core observations were supplemented onshore by scanning electron microscope observations on selected samples, using a VEGA3 TESCAN Scanning Electron Microscope in backscatter electron imaging mode with an accelerating voltage of 20 kV and a working distance of 16.8 mm.

Whole-rock geochemistry

serpentinized peridotites were selected by the Expedition 399 Shipboard Scientific Party as representative of the rocks recovered at Site U1601 (6 at Hole U1601A and 29 at Hole U1601C) for shipboard bulk rock geochemical analyses. They comprised 31 harzburgites, two opx-bearing dunites and two dunites. A thin section or an XRD sample was located next to each geochemistry rock sample to determine its modal composition and degree of alteration.

The 35 serpentinized peridotite samples were prepared from 30 to 150 cm³ of rock cut from cores and their outer surfaces cleaned to remove altered rinds resulting from drilling and cutting, then crushed according to the D/V JOIDES Resolution protocols (e.g., (61)). Crushed chips were ground to a fine powder using a SPEX 8515 Shatterbox powdering system with a tungsten carbide mill, except for five of the Hole U1601C samples that were powdered at Géosciences Montpellier using a Fritsch Pulverisette 2 with agate mortar and bowl. After powdering, each sample was ignited for 4 h at 1025°C to determine weight loss on ignition (LOI).

Bulk rock major and minor element analyses were conducted on splits of ignited powders using inductively coupled plasma optical emission spectroscopy (ICP-OES) on an Agilent 5110 spectrometer on-board D/V JOIDES Resolution for Hole U1601A samples and for 24 Hole U1601C samples, and on a Thermofisher iCAP Duo 7400 spectrometer at the AETE-ISO analytical facility (OSU OREME, University of Montpellier) for the five remaining Hole U1601C samples.

On board the D/V JOIDES Resolution, the digestion of rocks and subsequent ICP-OES analyses followed the protocol described in (62), summarized hereafter. 100.0 mg splits of whole-rock powders were mixed with LiBO₂ as a fluxer and LiBr as a non-wetting agent, then fused in Pt-Au crucibles in an internally rotating induction furnace (Bead Sampler NT-2100). The beads were dissolved in a 10% HNO₃ solution, then diluted to a dilution factor of ca. 5000. Be, In and Sb were used as an internal standard to correct for drift and matrix effects. Nine certified reference materials and one blank were prepared following the same protocol and used as calibration solutions.

At the AETE-ISO facility, 100 mg of rock powder was weighted and mixed with LiBO₂ and LiBr. Alkali fusion was conducted at 1000°C for 15 min using a Katanax X600 fluxer. After fluxing, the melt was mixed with 10% HNO₃ and diluted to a dilution factor of ca 2000. Sc was used as an internal standard. Six certified reference materials and one blank were prepared following the same protocol and used as calibration solutions.

Natural Gamma Radiation (NGR)

Gamma rays are emitted from rocks primarily as a result of the radioactive decay of ⁴⁰K and the decay of isotopes in the decay series of ²³⁸U and ²³²Th. The natural gamma radiation (NGR) of the in situ formation surrounding the borehole was determined by wireline logging. The Hostile Environment Natural Gamma Ray Sonde (HNGS; Schlumberger) measures natural radioactivity in the borehole wall using two bismuth germanate scintillation detectors. Concentrations of K, Th, and U, whose radioactive isotopes dominate the natural radiation spectrum, were computed by Schlumberger's proprietary spectroscopy method. The tool string was sent to the bottom of the hole while recording a partial set of data and was then pulled up at a constant speed (typically 250–500 m/h) to acquire the reported data.

The HNGS was deployed on four separate tool string deployments, yielding highly correlative profiles of computed K, Th, and U concentrations. In order to stabilize the drill string during wireline logging, the lowermost few tens of meters are stationary inside the borehole and the topmost 20-30 m of data logged through the pipe are invalid. The logging depth scale (WMSF = Wireline log matched depth below sea floor) is slightly different from the coring depth scale (typically up to a few dm discrepancy at any stratigraphic level) due to the different tools and methods used to measure and compute depth, respectively.

The HNGS Standard (total) Gamma Ray (HSGR) data is reported in standard gamma ray units of the American Petroleum Institute (gAPI). The HNGS Computed Gamma Ray (HCGR) data is the HSGR minus the uranium component.

5

Moisture and density (MAD)

Mass and volume measurements on discrete samples were made to determine bulk, dry, and grain density. The method is IODP standard for hard rocks and consists of a vacuum water saturator, a dual balance system, and a custom-built Helium hexapycnometer.

- 10 After saturating the cube samples with seawater, the wet mass was measured. The samples were subsequently dried in a 105°C oven for 24 h and then cooled to room temperature in a desiccator for 3 h, after which their dry mass was obtained for MAD measurements. The volume of the dry cube samples was then obtained using Helium pycnometry. Bulk density, dry density, and grain density were then calculated from wet mass, dry mass, and dry volume measurements using IODP Method C (63).

15

Dual balance system

A dual balance system was used to measure both wet and dry masses. Two analytical balances (Mettler-Toledo XS204) compensate for ship motion; one acts as a reference and the other measures the sample. The discrete samples were placed in aluminum trays, which were used to tare the reference and unknown balances. A standard mass of similar mass to that of the sample was placed on the reference balance to increase accuracy. Using a reference mass within ~10% of the sample mass, an accuracy of 0.005 g is readily attainable.

20

Hexapycnometer system

The hexapycnometer is an IODP custom-built system, using six Micromeritics cell units, custom electronics, and custom control programs. The system measures dry sample volume using pressurized Helium-filled chambers with a precision of 0.02 cm³. For each measurement series, five cells contained unknowns and one cell contained two stainless steel calibration spheres (3 and 7 cm³) with a total volume of ~10 cm³. Calibration spheres were cycled through the cells to identify any systematic error and/or instrument drift. Spheres are assumed to be known to within 1% of their total volume. Three Helium purge cycles were carried out for each sample for increased accuracy.

25

30

Moisture and density calculations

For density calculations, both mass and volume are first corrected for the salt content of the pore fluid:

$$35 \quad M_s = [S(M_w - M_d)] / (1 - S) \quad (1)$$

where

- M_s = mass of salt,
- S = pore water salinity, (seawater with salinity 35 psu or 0.035 g/cm³),
- M_w = wet mass of the sample, and
- 40 • M_d = dry mass of the sample.

Grain density (ρ_g) is determined from the dry mass (M_d) and dry volume (V_d) measurements:

$$\rho_g = (M_d - M_s) / [V_d - M_s / \rho_s] \quad (2)$$

- 45 where ρ_s is the density of salt (2.20 g/cm³) (63).

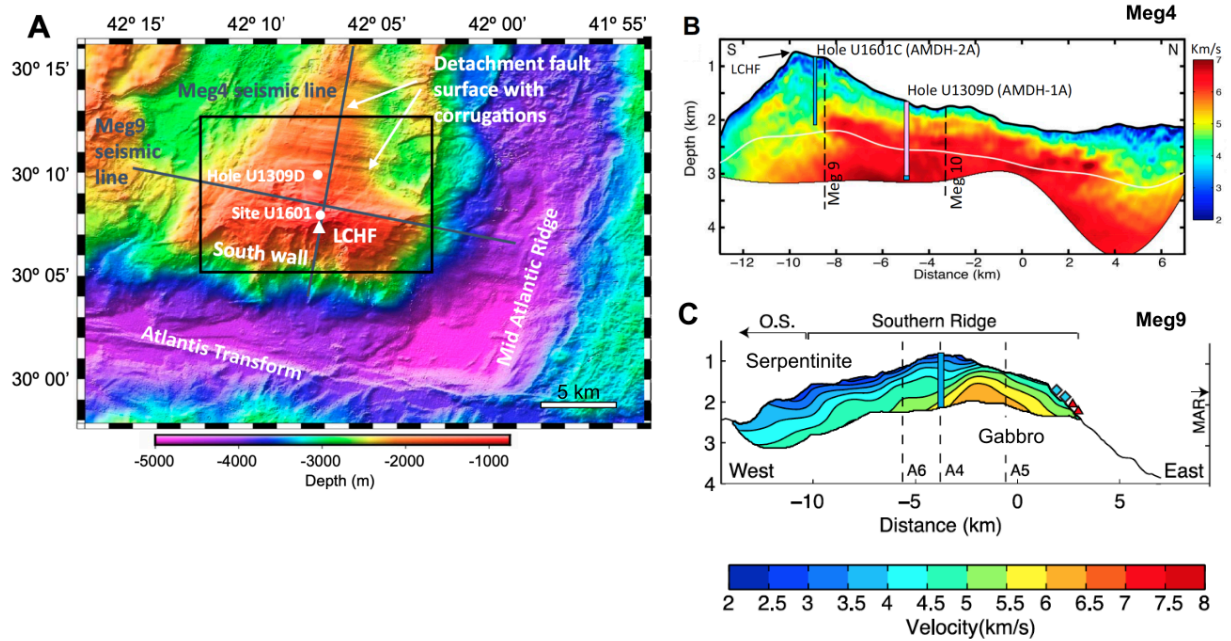


Fig. S1: The Atlantis Massif, seismic data, and IODP drilling. (A) Bathymetric map (15) showing the Atlantis Massif, seismic lines, the corrugated detachment fault surface, the Lost City hydrothermal field (LCHF) and IODP drilling locations. (B) Meg4 seismic line with full waveform inversion (FWI) processing, modified from (64). The solid white line marks the limit of the ray coverage for the tomographic inversion. Hole U1309D, drilled in IODP Expeditions 304/305 (14), was deepened by 80m during Expedition 399. Hole U1601C and a 55m pilot hole (U1601A) were drilled during Expedition 399. (C) Meg9 seismic line (65), with Hole 1601C shown. FWI has not been published for this line. In both this and Meg4, velocities >6km/s are assumed to be gabbro. Blue squares on the slope indicate dredge samples of gabbro exposed on the seafloor.

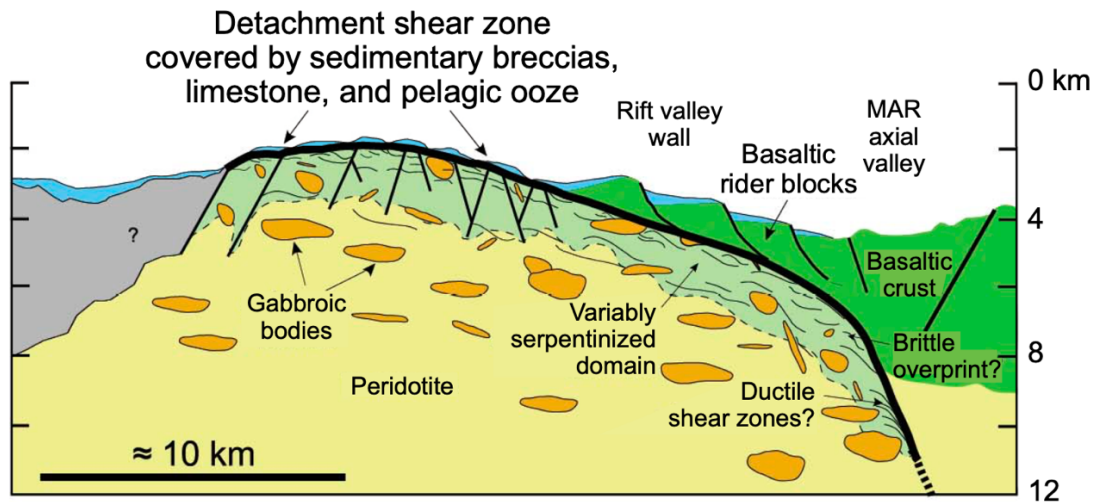


Fig. S2: Cross section of the South wall of Atlantis Massif. The South wall is dominated by variably altered peridotites with gabbroic lenses. Estimated 100 m thick detachment fault zone containing talc-tremolite-chlorite metasomatic schists is at the summit (16). In Expedition 399, the fault zone was found to be <30 m thick. MAR = Mid-Atlantic Ridge. Modified from (66).

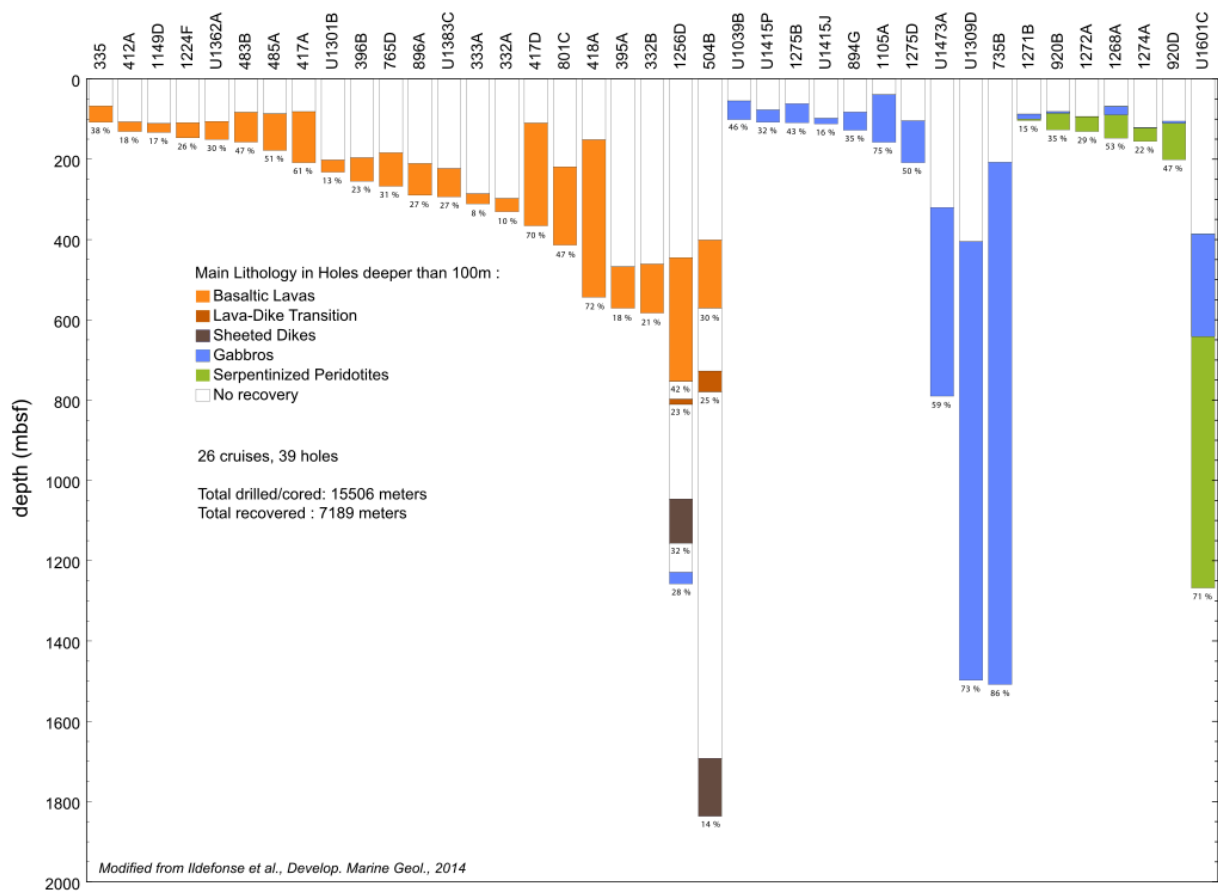


Fig. S3: Previous drilling of oceanic crust. Summary of all DSDP/ODP/IODP holes >100m in depth in igneous basement, modified from (67). Hole U1601C is more than six times as deep as the previous record in serpentinized peridotite.

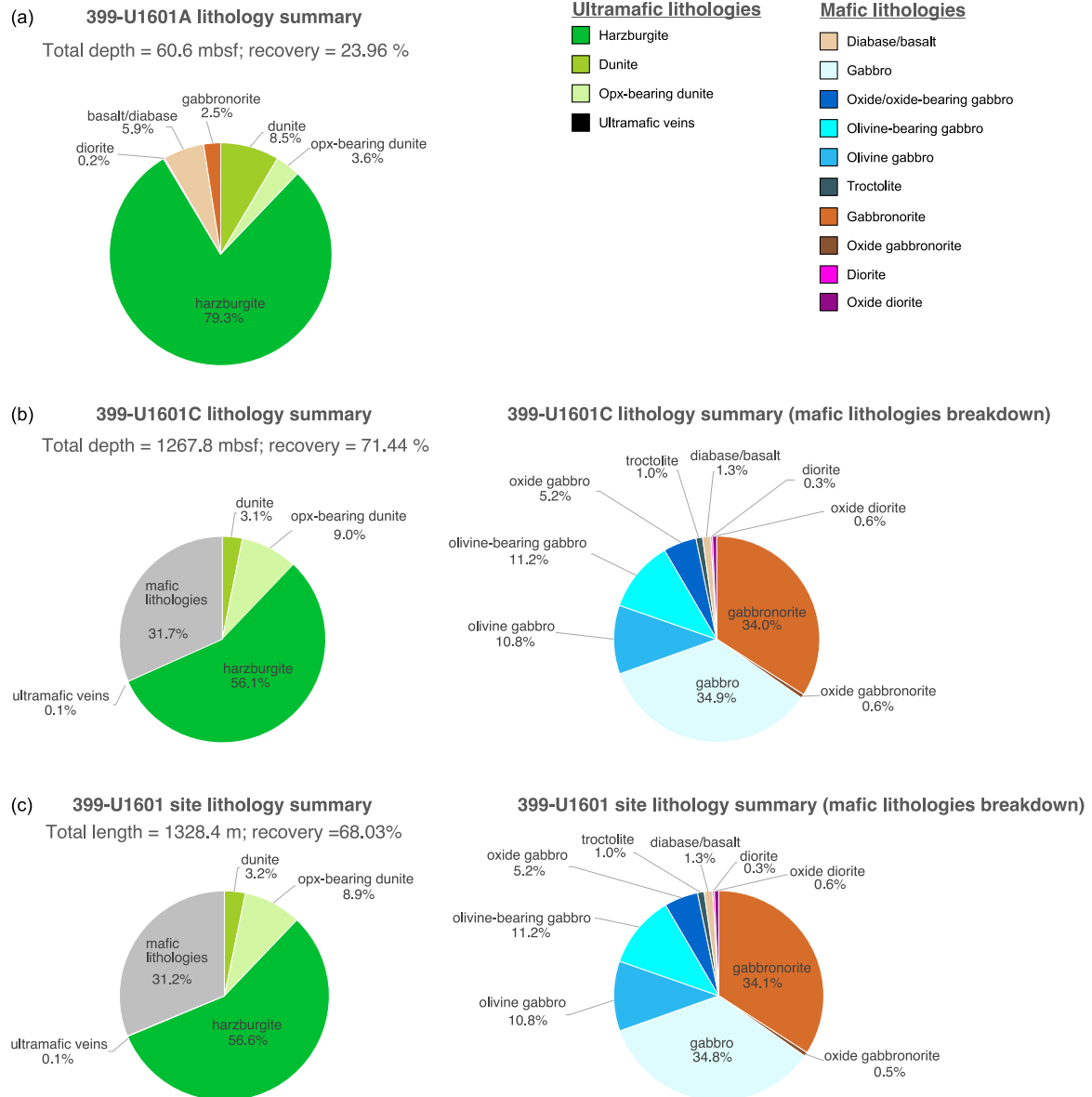


Fig. S4: lithological percentages of rocks recovered from Hole U1601A (A), Hole U1601C (B) and Site U1601 (C).

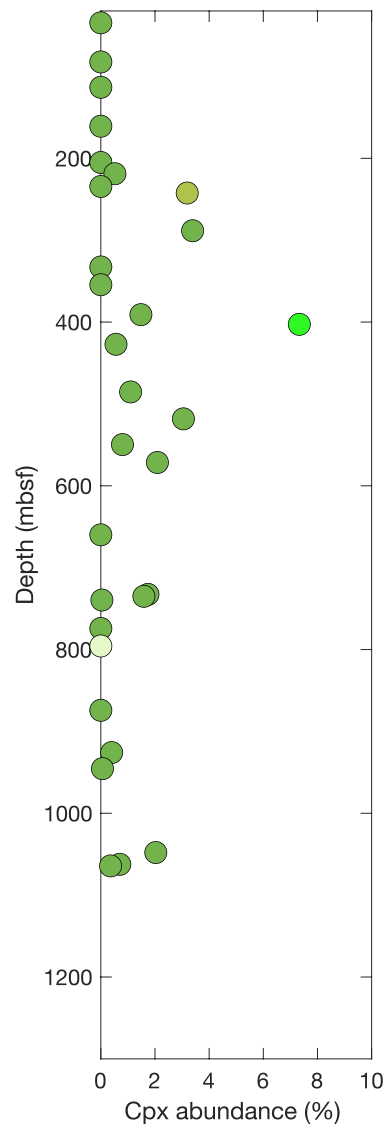


Fig. S5: Downhole model abundance (%) of clinopyroxene from digital point counting.

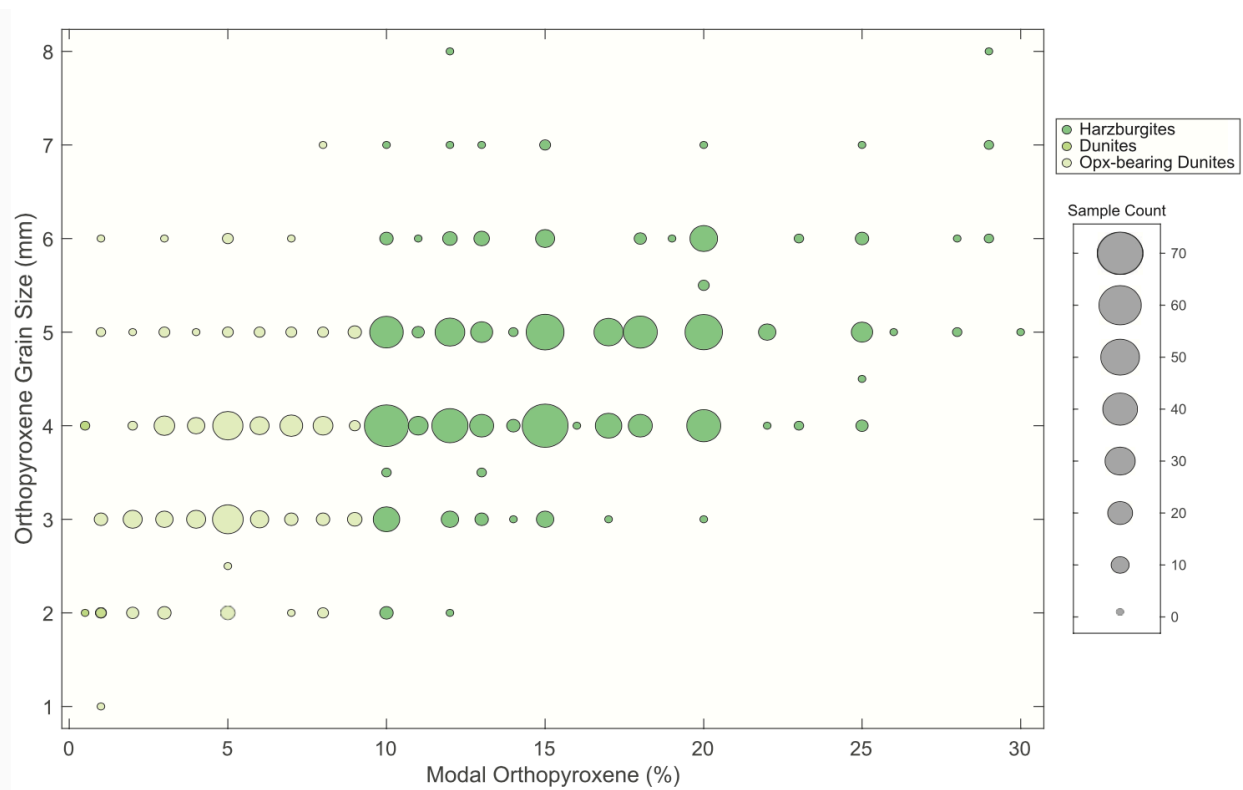


Fig. S6: Orthopyroxene size-abundance relationships. Data are for Hole U1601C harzburgite, opx-bearing dunite and dunite. Symbol size is proportional to number of datapoints.

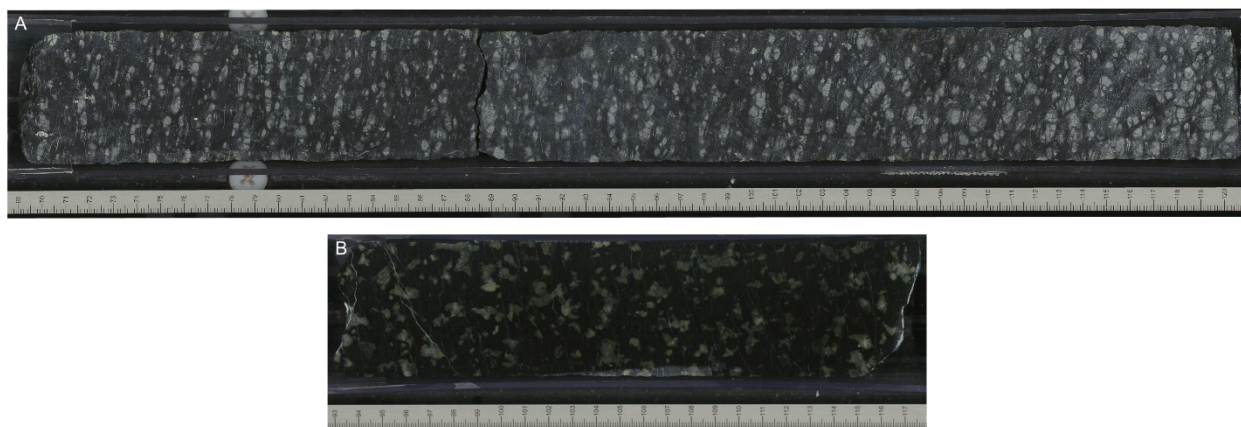


Fig. S7: Mantle fabrics. (A) Strongly foliated porphyroclastic harzburgite (Interval 399-U1601C-148R-3, 69 -121 cm). **(B)** Protogranular harzburgite (Interval 399-U1601C-113R-4, 93 -117 cm).

5

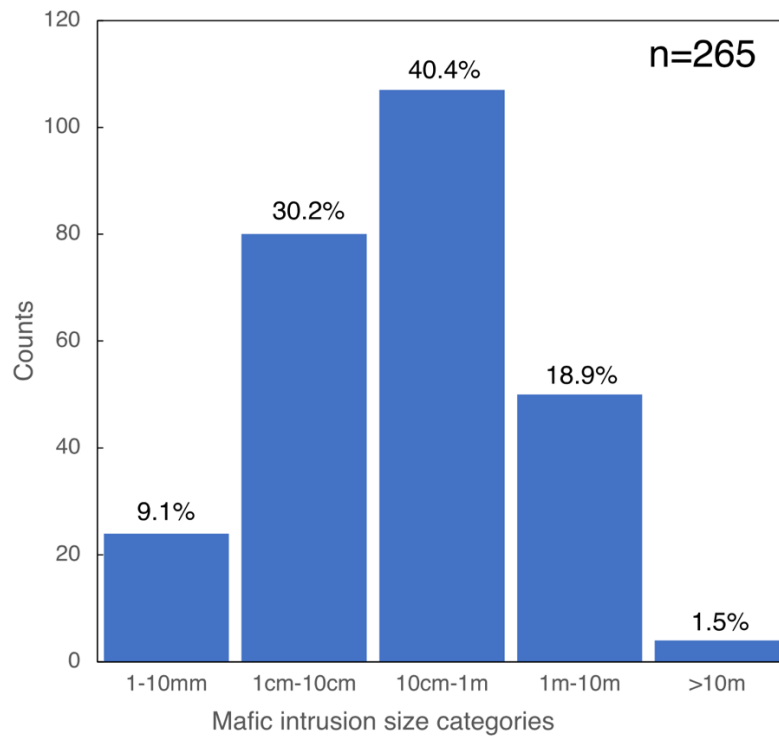


Fig. S8: Size distribution of gabbroic intrusions in Hole U1601C

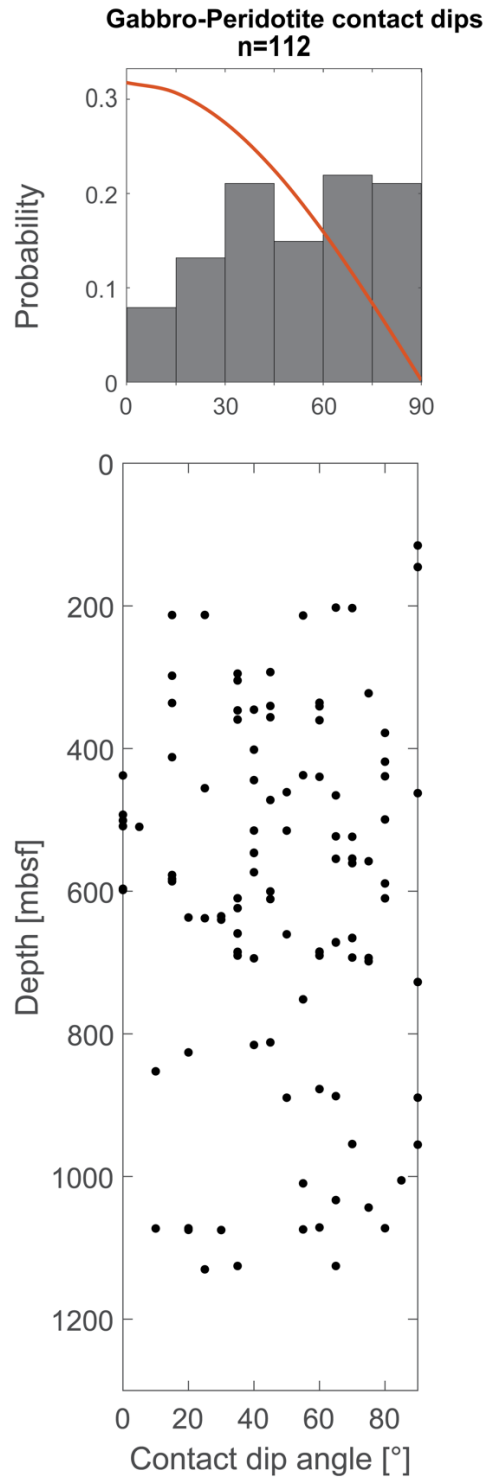


Fig. S9: Gabbro-peridotite dips. Histogram and downhole distribution of dip of gabbro-peridotite contacts in Hole U1601C. The distribution predicted for randomly orientated planes in drill core in red is superimposed on the histogram (50).

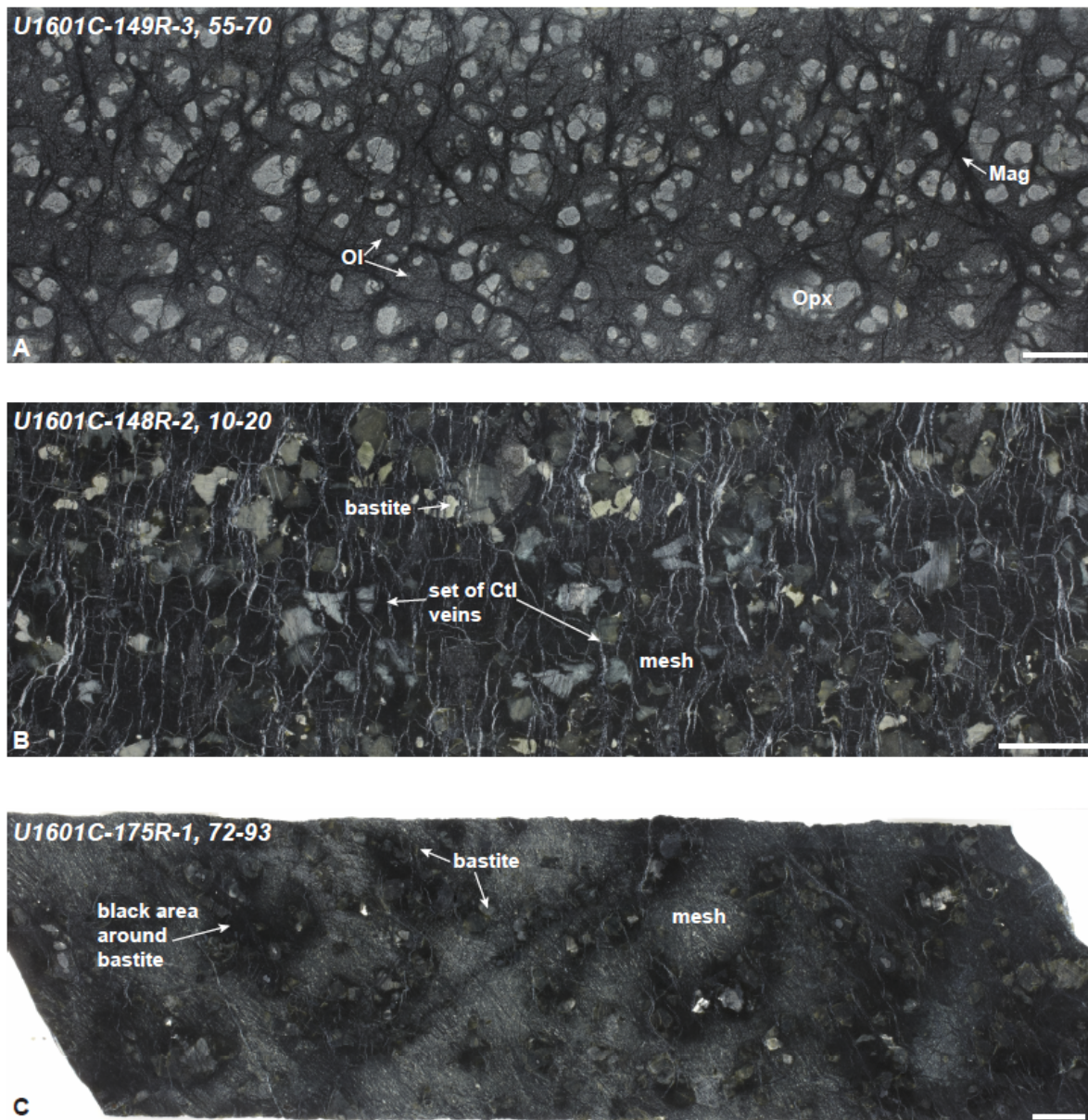


Fig. S10: Variably serpentinized peridotite in Hole U1601C. (A) Serpentinized harzburgite with common orthopyroxene and olivine relicts. Note that chrysotile veins are absent (Interval 399-U1601C-149R-3, 55-70 cm). (B) Highly serpentinized (~90%) harzburgite containing green and grey bastite after orthopyroxene. A set of white, fibrous to massive, subparallel horizontal anisgranular to locally paracrystalline chrysotile (Ctl) veins crosscuts the serpentinized harzburgite (Interval 399-U1601C-148R-2, 10-20 cm). (C) Highly serpentinized harzburgite (>90%) containing black and grey bastite after orthopyroxene. Black areas are commonly found around bastite. The serpentinite is cut by a few chrysotile veins (Interval 399-U1601C-175R-1, 72-93 cm). The white bar is 1 cm.

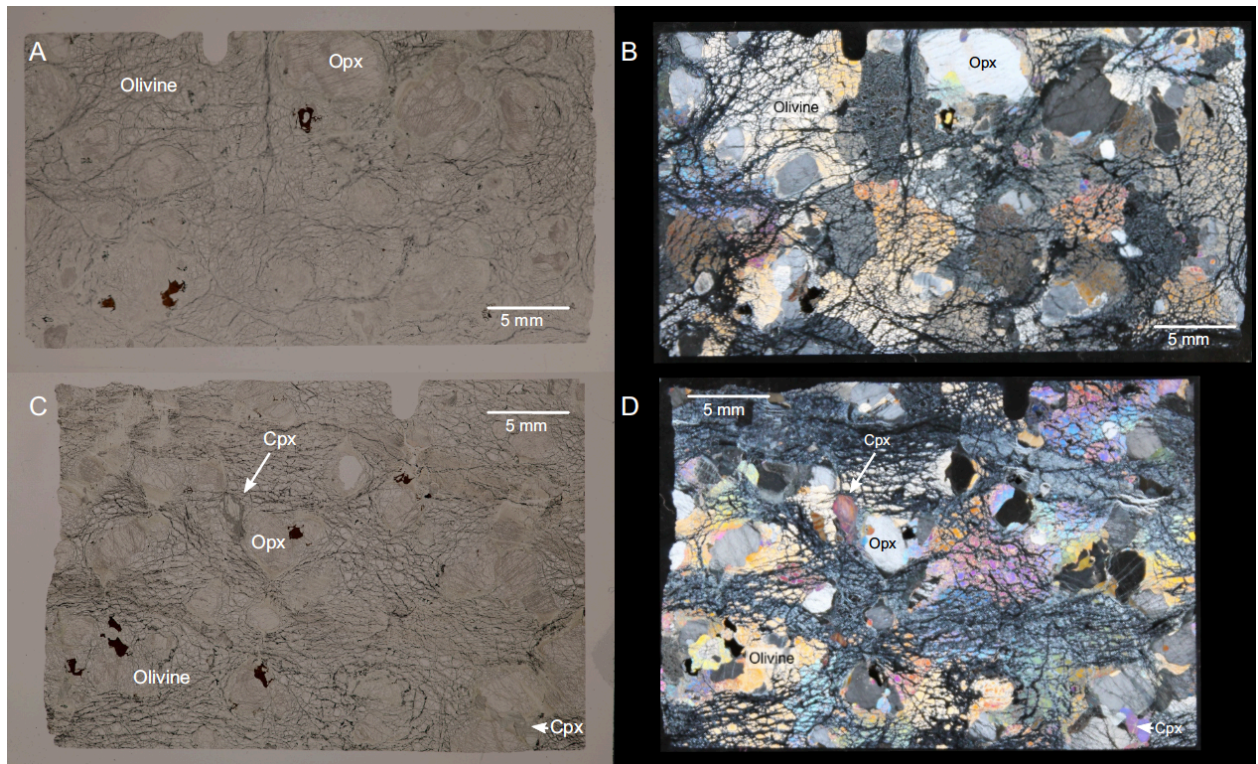


Fig. S11: Relatively fresh harzburgite. Whole thin section images (plane- and cross-polarized light) of Interval 399-U1601C-149R-3, 94-97 cm (**A, B**) and Interval 399-U1601C-148R-3, 118-121 cm (**C, D**) show abundant relict olivine and largely fresh orthopyroxene (opx) and sparse clinopyroxene (cpx) in harzburgite.

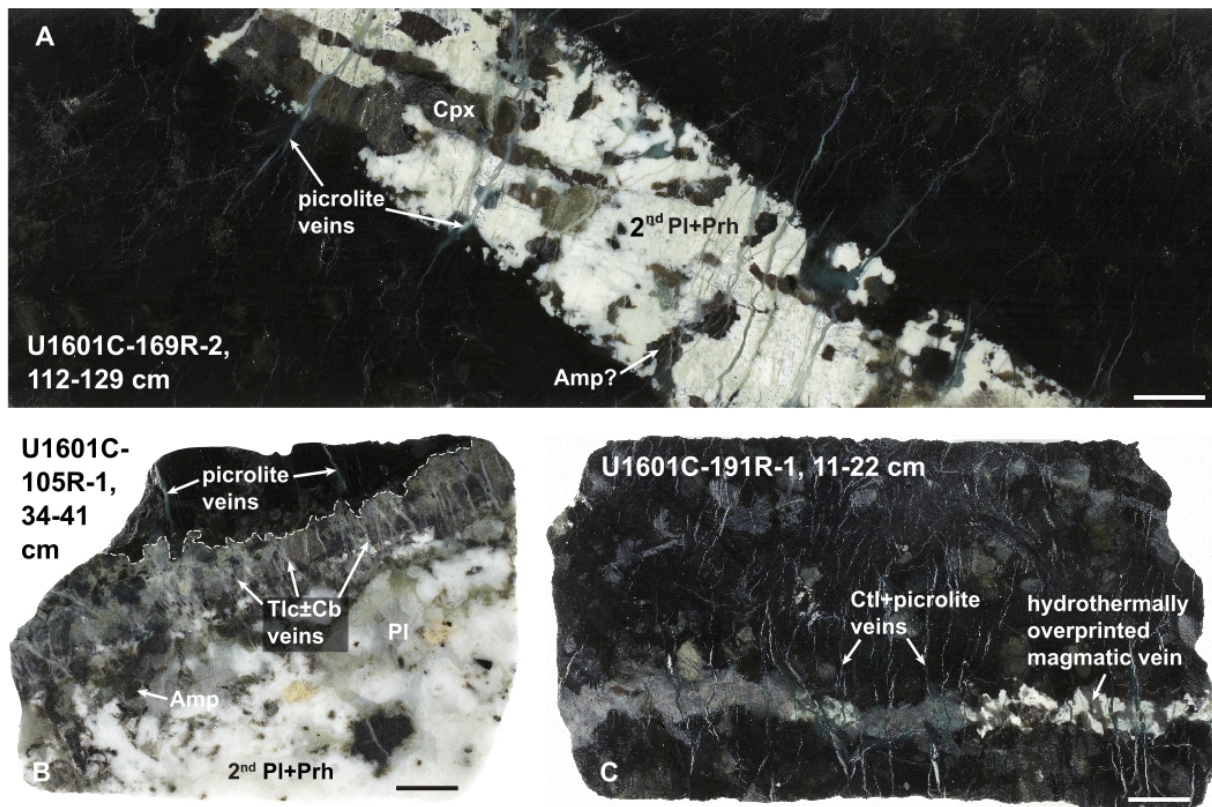


Fig. S12: Close-up images of the main vein type occurrences in serpentinized peridotites and at serpentinized peridotite-gabbroic rock contacts in Hole U1601C. (A)

- 5 Hydrothermally overprinted magmatic vein composed of clinopyroxene (Cpx), amphibole (Amp?), prehnite (Prh), and secondary plagioclase (Pl) cut by a set of green massive picrolite veins (Interval 399-U1601C-169R-2, 112-129 cm). (B) Contact between serpentinized peridotite and altered gabbro (Interval 399-U1601C-105R-1, 34-41 cm). Set of talc (Tlc)-carbonate (Cb) veins branches at the contact and further continues in gabbro but not in serpentinite. A few picrolite veins cut through serpentinite and grade into prehnite veins when propagating in gabbro. (C) Hydrothermally overprinted magmatic vein cut by a set of composite chrysotile-picrolite veins (Interval 399-U1601C-191R-1, 11-22 cm). Picrolite vanishes away from magmatic vein.
- 10

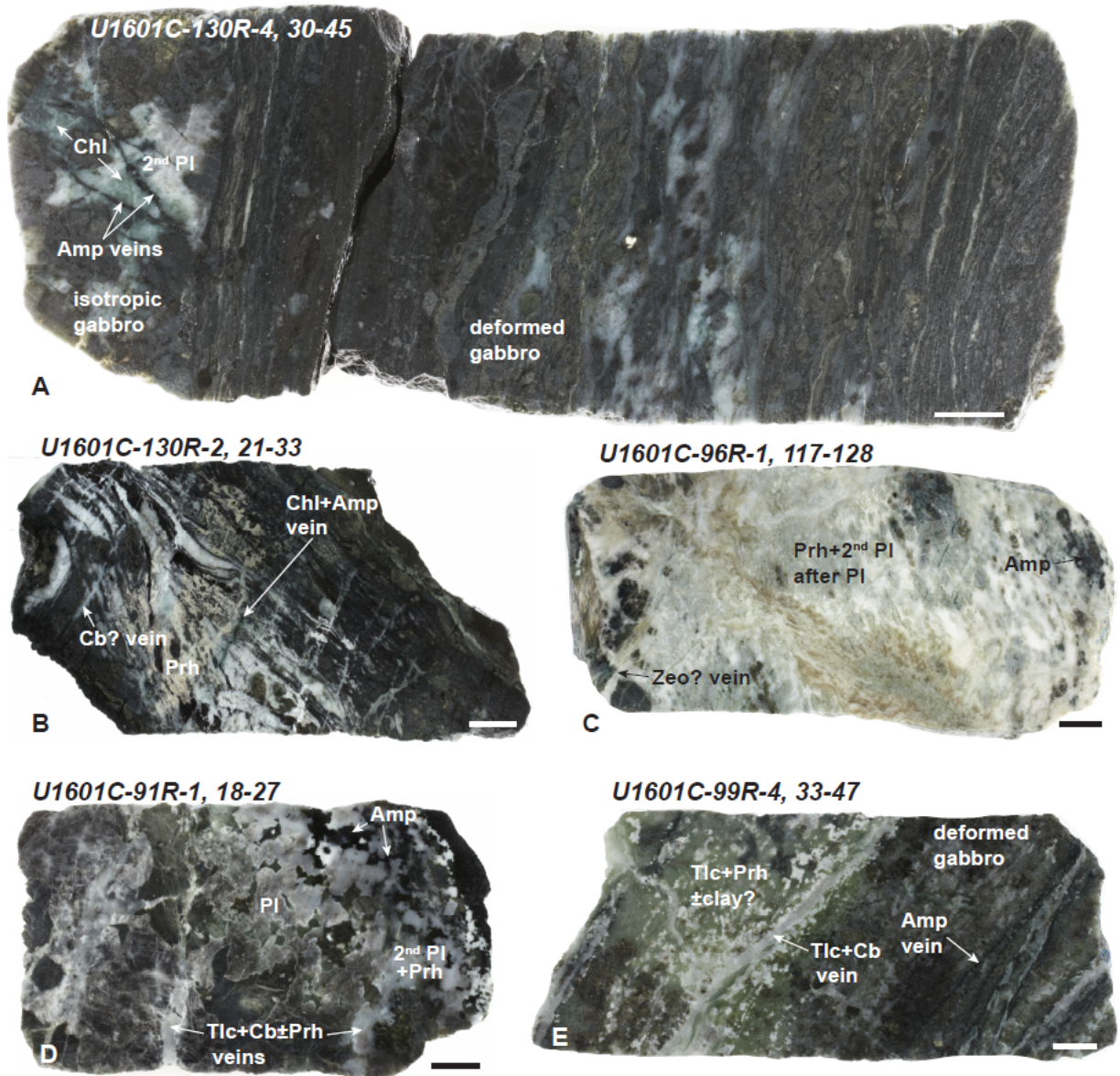


Fig S13. Close-up images of the main alteration features of gabbroic rocks in Hole U1601C. (A) Contact between a ductily-deformed and isotropic gabbro. Amphibole veins cut through the isotropic gabbro. Secondary plagioclase and chlorite form after plagioclase (Interval 399-U1601C-130R-4, 30-45 cm). (B) Highly deformed and altered (prehnite) gabbro cut by chlorite-amphibole veins overprinted by late carbonate(?) veins (Interval 399-U1601C-130R-2, 21-33 cm). (C) Highly altered and bleached gabbro composed of amphibole, secondary plagioclase, and prehnite and cut by late possible zeolite veins (Interval 399-U1601C-97R-1, 117-128 cm). (D) Contact between altered gabbro and serpentinized peridotite. Towards the contact, the degree of alteration in the gabbro increases and igneous minerals are completely replaced by amphibole, secondary plagioclase, and prehnite. It is cut by late talc-carbonate-prehnite veins (Interval 399-U1601C-91R-1, 18-27 cm). (E) Talc-carbonate veins cutting through a deformed gabbro. Talc, prehnite, and possibly clay minerals pervasively replace the gabbro at the vicinity of the veins (Interval 399-U1601C-99R-4, 33-47 cm). The scale bars are 1 cm.



Fig. S14: Highly weathered and serpentized peridotite. Fe-(oxy)hydroxide veins locally reuse former serpentine veins and cut through the serpentine-magnetite veins (mesh network) and bastite suggesting weathering postdates serpentinization (Interval 399-U1601C-27R-1, 28-55 cm).

5

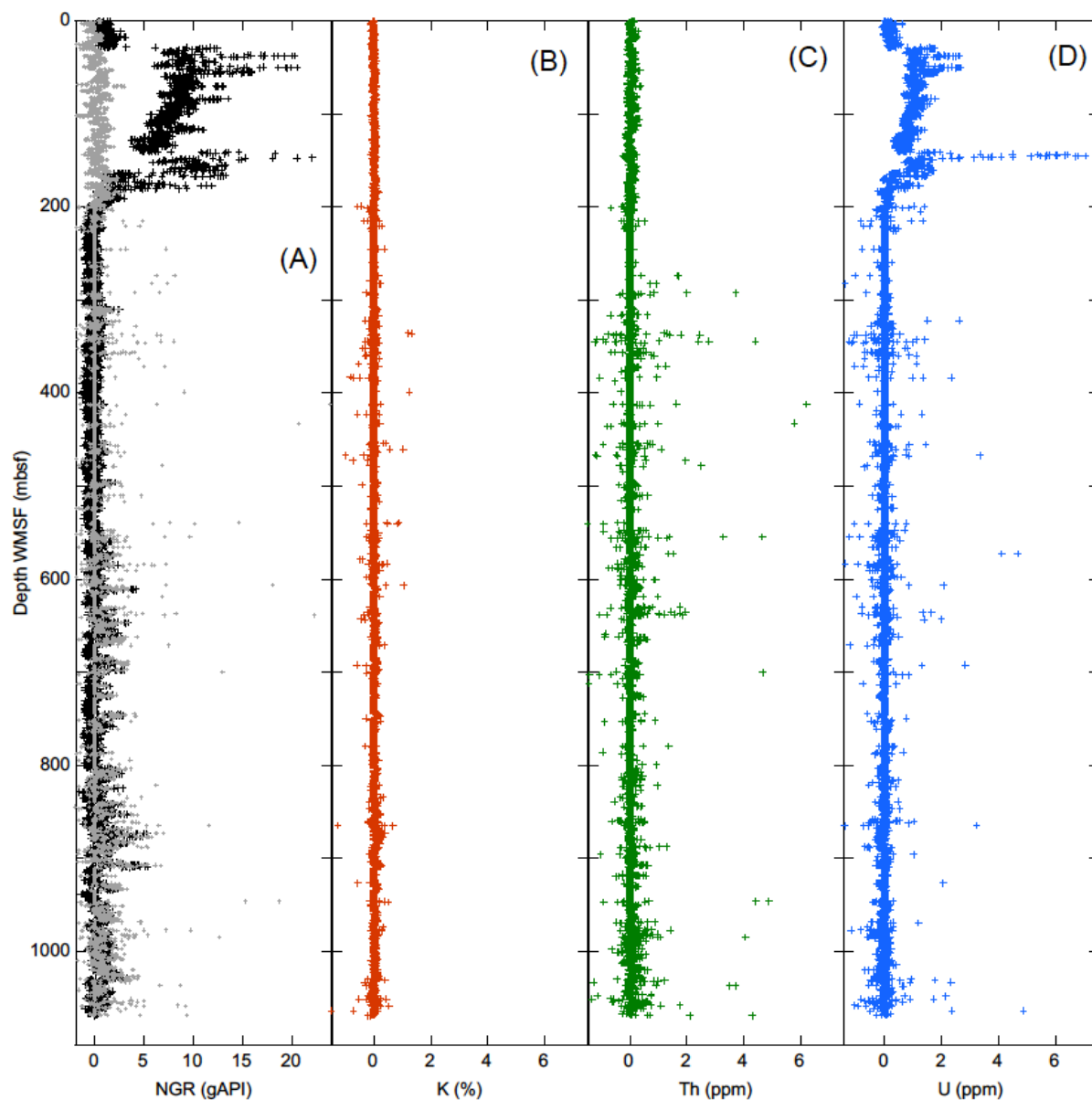


Figure S15. Wireline natural gamma ray (NGR) data. (A) Total signal (HSGR, black) and the computed signal without the uranium component (HCGR, gray). Concentrations of (B) potassium (C) thorium and (D) uranium computed by Schlumberger's proprietary spectroscopy method.

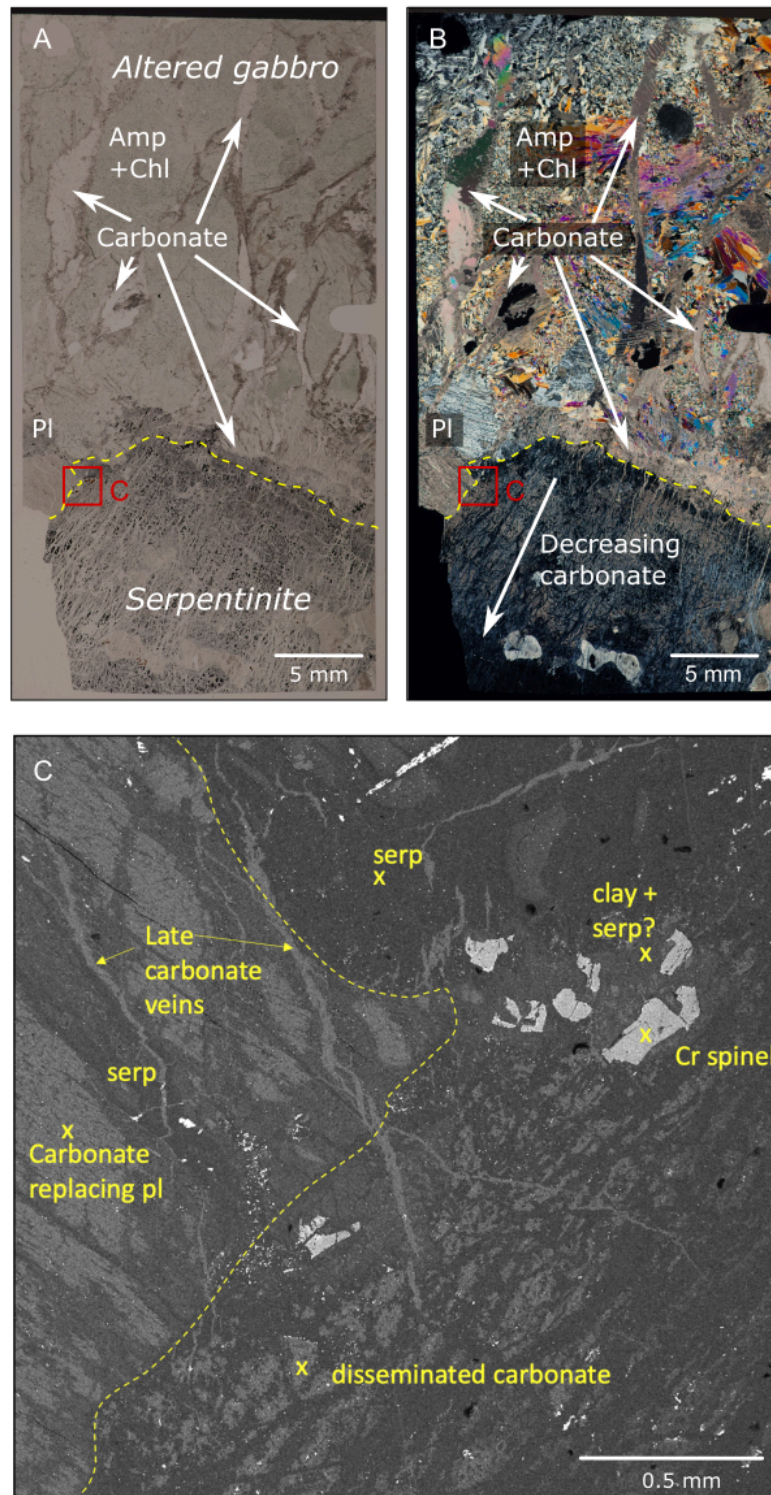


Fig. S16: Extensive carbonate veining and alteration in serpentinized peridotite and altered gabbro. Interval 399-U1601C-177R-1, 35-38 cm. (A) Whole thin section image

(plane-polarized light) showing carbonate veins cutting gabbro completely altered to amphibole (Amp), chlorite (Chl), clay minerals, and locally secondary plagioclase, in contact with highly serpentinized peridotite. The contact is highlighted by the yellow dashed line. (B) Cross-polarized light image showing coarse amphiboles and a relict plagioclase grain (Pl), altered to secondary plagioclase. Location of panel (C) is shown, and the decrease in disseminated and vein carbonate away from the contact can be seen by the reduction in birefringence. (C) Backscatter SEM image showing the boundary between gabbro and

serpentinized peridotite. Disseminated calcium carbonate (EDS analysis shows no magnesite is present) is interpreted to overprint serpentine (serp) in the ultramafic layer. Cr-spinel is altered to serpentine and clay/chlorite. In the gabbro layer, a plagioclase grain (small relicts visible beyond the field of view) is almost completely altered to carbonate, serpentine, and probably chlorite. Thin carbonate veins cut the contact, indicating that they represent the latest event.